

1 Meteorological modeling sensitivity to parameterizations and 2 satellite-derived surface datasets during the 2017 Lake Michigan 3 Ozone Study

4 Jason A. Otkin^{1,2}, Lee M. Crounce^{1,2}, Jonathan L. Case³, R. Bradley Pierce¹, Monica Harkey⁴, Allen
5 Lenzen¹, David S. Henderson¹, Zac Adelman⁵, Tsengel Nergui⁵, Christopher R. Hain⁶
6

7 ¹Space Science and Engineering Center, University of Wisconsin-Madison, Madison, 53706, USA
8 ²Cooperative Institute for Meteorological Satellite Studies, University of Wisconsin, Madison, Madison, 53706, USA
9 ³ENSCO, Inc., NASA Short-term Prediction Research and Transition Center, Huntsville, 35805, USA
10 ⁴Center for Sustainability and the Global Environment, University of Wisconsin-Madison, Madison, 53706, USA
11 ⁵Lake Michigan Air Directors Consortium, Hillside, 60162, USA
12 ⁶Earth Science Office, NASA Marshall Space Flight Center, Huntsville, 35808, USA
13

14 Correspondence to: Jason A. Otkin (jasono@ssec.wisc.edu)

15 **Abstract.** High-resolution simulations were performed to assess the impact of different parameterization schemes, surface
16 datasets, and analysis nudging on lower-tropospheric conditions near Lake Michigan. Simulations were performed where
17 climatological or coarse-resolution surface datasets were replaced by high-resolution, real-time datasets depicting lake surface
18 temperatures (SST), green vegetation fraction (GVF), and soil moisture and temperature (SOIL). Comparison of two baseline
19 simulations employing different parameterization schemes (referred to as “AP-XM” and “YNT”, respectively) showed that
20 the AP-XM simulation produced more accurate analyses on the outermost 12-km resolution domain, but that the YNT
21 simulation was superior for higher-resolution nests. The diurnal evolution of the surface energy fluxes was similar in both
22 simulations on the 12-km grid but differed greatly on the 1.3-km grid where the AP-XM simulation had much smaller sensible
23 heat flux during the daytime and physically unrealistic ground heat flux. Switching to the YNT configuration led to more
24 accurate 2-m temperature and 2-m water vapor mixing ratio analyses on the 1.3-km grid. Additional improvements occurred
25 when satellite-derived surface datasets were incorporated into the modeling platform, with the SOIL dataset having the largest
26 positive impact on temperature and water vapor. The GVF and SST datasets also produced more accurate temperature and
27 water vapor analyses, but degradations in wind speed, especially when using the GVF dataset. The most accurate simulations
28 were obtained when using the high-resolution SST and SOIL datasets and analysis nudging above 2 km AGL. These results
29 demonstrate the value of using high-resolution satellite-derived surface datasets in model simulations.

30 1 Introduction

31 Locations along the Lake Michigan shoreline in the United States have a long history of recording surface ozone concentrations
32 that exceed levels set by the National Ambient Air Quality Standards (NAAQS), especially during the warm season (Stanier
33 et al. 2021). Since the first ozone NAAQS was released in 1979, most lakeshore counties in the states bordering Lake Michigan
34 (Wisconsin, Illinois, Indiana, and Michigan) have been designated as being in nonattainment for surface ozone in one or more
35 of the subsequent NAAQS revisions. These states are required by the Clean Air Act to develop State Implementation Plans

- Deleted: initialization
- Deleted: run
- Deleted: initialization
- Deleted: a
- Deleted: a configuration similar to that used at the Environmental Protection Agency (“EPA”) to another simulation employing an alternative...
- Deleted: set of
- Deleted: EPA
- Deleted: configuration
- Deleted: configuration
- Deleted: EPA
- Deleted: substantial decreases in root mean square error for
- Deleted: the high-resolution

50 (SIPs) to demonstrate strategies to bring affected areas into attainment and to mitigate the impacts of high ozone
51 concentrations. Large decreases in local emissions of ozone precursors such as nitrogen oxides and volatile organic compounds
52 have steadily reduced one- and eight-hour maximum ozone concentrations across the region in recent decades (Adelman 2020).
53 However, the implementation of stricter ozone NAAQS means that additional air quality modeling assessments are necessary
54 to help states demonstrate that they can reach attainment by the required statutory deadlines.
55

56 Urban and rural areas near Lake Michigan are susceptible to high ozone events due to the complex interaction between synoptic
57 and mesoscale circulation patterns with large sources of industrial, transportation, and urban emissions along the southern end
58 of the lake. High ozone days are most common when synoptic-scale weather patterns characterized by weak southerly winds
59 transport ozone and its precursors northward from their primary source regions over the Chicago and Milwaukee metropolitan
60 areas and then interact with the mesoscale lake and land breeze circulations (Lyons and Olsson 1973; Ragland and Samson
61 1977; Lennartson and Schwartz 2002). At night, the land breeze carries ozone precursors from land-based emissions sources
62 over the lake where they become confined within a shallow nocturnal boundary layer and are then converted into ozone after
63 sunrise via photochemical processes (Dye et al. 1995). As the land surface warms during the day, a reversal of the mesoscale
64 circulation leads to the formation of the lake breeze during the morning that transports the high ozone airmass back onshore,
65 with elevated ozone concentrations occurring across inland areas during midday and afternoon. On high ozone days, the lowest
66 ozone concentrations are often found in areas with high nitrogen oxide emissions, such as Chicago and northwestern Indiana,
67 with the highest ozone levels located downwind in rural and suburban areas to the north of these urban and industrial locations
68 (Foley et al. 2011; Cleary et al. 2015).
69

70 When synoptic-scale conditions are favorable for lake and land breeze formation, the horizontal temperature gradient between
71 adjacent land and water areas influences the strength of the circulation pattern and the distance that the lake breeze penetrates
72 inland during the daytime. Changes in the location of the lake breeze can have a profound impact on near-surface meteorology,
73 the depth and vertical structure of the planetary boundary layer (PBL), and ozone concentrations along the Lake Michigan
74 shoreline (Dye et al. 1995). Among other things, an accurate depiction of near-surface features in numerical weather prediction
75 models requires an accurate specification of lower boundary conditions at the land and water surface. For example, an accurate
76 representation of land surface conditions (such as soil moisture, soil temperature, and green vegetation fraction) are necessary
77 to correctly partition the surface net radiation into sensible, latent, and ground heat fluxes. This partitioning in turn impacts
78 the growth and depth of the PBL and lower-tropospheric temperature, moisture, and wind profiles (Berg et al. 2014; Dirmeyer
79 and Halder 2016; Schwingshaki et al. 2017; Welty and Zeng 2018). Soil moisture and vegetation fraction (or leaf area index)
80 are especially important variables through their influence on land-atmosphere coupling processes that link the surface
81 hydrologic and atmospheric components of the earth system (Santanello et al. 2018, 2019). Indeed, Huang et al. (2017) showed
82 that use of improved soil moisture and green vegetation fraction estimates in high-resolution simulations reduced biases in air
83 temperatures and PBL heights over the Missouri Ozarks and had a large impact on biogenic isoprene emissions.
84

85 Given the important role that boundary layer meteorology and the land-lake breeze circulation have on ozone production and
86 transport in the Lake Michigan region, it is critical to explore the ability of different parameterization schemes and surface
87 datasets to improve the accuracy of near-surface meteorological and air quality simulations. For example, ozone production is
88 highly sensitive to temperature and humidity (Bloomer et al. 2009; Camalier et al. 2007; Coates et al. 2016; Dawson et al.
89 2007; Jacob and Winner, 2009; Pusede et al. 2015), and production and transport of ozone precursors such as nitrogen oxides
90 and volatile organic compounds are also dependent on temperature and winds (Dye et al. 1995; Porter and Heald, 2019; Wang
91 et al. 2022; Wiedinmyer et al. 2006). In this two-part study, we develop and assess the accuracy of a satellite-constrained
92 modeling platform for the Midwest United States that supports the needs of the Lake Michigan Air Directors Consortium
93 (LADCO) as they conduct detailed air quality modeling assessments for its member states. The modeling platform uses high-
94 resolution analyses of soil moisture, green vegetation fraction, and lake surface temperatures derived from satellite
95 observations and an offline land surface model (LSM) to constrain the evolution of the lower boundary conditions during
96 multi-week model simulations. In part I, we use results from a large set of Weather Research and Forecasting (WRF) model
97 simulations to assess the impact of the high-resolution surface datasets, different parameterization schemes, and analysis
98 nudging on near-surface meteorological conditions and energy fluxes. We will show that a baseline model configuration
99 employing default surface datasets produces better results for model simulations performed at 12-km horizontal grid spacing,

Deleted: initialization

Formatted: Font: 10 pt

Deleted:

Deleted: and parameterization schemes similar to those used by the United States Environmental Protection Agency (EPA)

04 but that more accurate results are obtained at higher resolutions when the satellite-derived surface datasets and alternative
05 parameterization schemes are used. In part II of this study, we use meteorological analyses from two of the WRF model
06 configurations as input to Community Multiscale Air Quality (CMAQ) model simulations to assess the impact of these model
07 changes on ozone forecasts in the Lake Michigan region. The remainder of this paper is organized as follows. Section 2
08 contains a description of the model configurations and surface datasets. Results are presented in Section 3, with a discussion
09 and conclusions provided in Section 4.

Deleted: initialization

Deleted: obtained

Deleted: the baseline EPA and optimized

Deleted: initialization

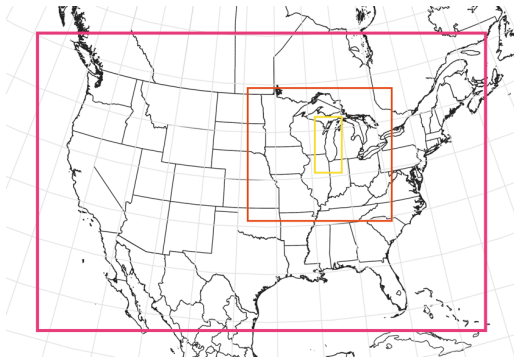
10 2. Methods

11 2.1 WRF model configurations

12 Version 3.8.1 of the WRF Preprocessing System (WPS) and WRF model (Powers et al. 2017) was used to perform simulations
13 containing three one-way nested domains covering the contiguous United States, Midwest United States, and Lake Michigan
14 regions with 12, 4, and 1.3 km horizontal resolutions, respectively (Fig. 1). Each simulation contained 40 terrain-following
15 vertical layers, with seven of the layers located below 2 km. The model top was set to 100 hPa. The 0.25-degree resolution
16 GFS Final reanalyses available at 6-h intervals served as initial and lateral boundary conditions (ICs/BCs) for the WRF model
17 simulations. All simulations were run from 12 May 2017 – 22 June 2017, with our evaluation focusing on the 22 May – 22
18 June 2017 time period corresponding to the Lake Michigan Ozone Study field project (Stainer et al. 2021). Except for the two
19 baseline simulations described below, all of the simulations were performed in daily increments using the standard WRF model
20 restart files to allow for daily updates of high-resolution surface datasets using the WPS. The 40-category National Land Cover
21 Dataset (NLCD) 2011 land use dataset (Jin et al. 2013) was used to determine the vegetation type and soil properties for each
22 model grid point.

Deleted: t

Deleted: analysis



24
25 **Figure 1.** Map showing the geographic regions covered by the 12-km (red box), 4-km (orange box), and 1.3-km (yellow box)
26 resolution domains used during the WRF model experiments.

27
28 Eight model simulations were performed to assess the impact of different physics options and surface datasets on the model
29 accuracy in the lower troposphere (Table 1). The first simulation, hereafter referred to as the “AP-XM” baseline configuration,
30 employed the Morrison microphysics (Morrison et al. 2005), RRTMG longwave and shortwave radiation (Iacono et al. 2008;
31 Mlawer et al. 1997), and ACM2 PBL (Pleim 2007) parameterization schemes on all three domains, along with the Kain-Fritsch
32 cumulus scheme (Kain 2004) on the outer two domains. These schemes were chosen for the baseline configuration because
33 they are often used in simulations performed at the U.S. Environmental Protection Agency (EPA). The ACM2 PBL scheme is

Deleted: initialization

Deleted: employed a configuration similar to that used in air quality modeling at the EPA and is

Deleted: EPA

Deleted: . This simulation

a hybrid first-order closure scheme that attempts to capture both local and non-local fluxes (Pleim 2007). When conditions are stable, only the local closure portion of the ACM2 scheme is used. Surface energy fluxes (sensible, latent, and ground) and changes in soil moisture and soil temperature were simulated using the Pleim-Xiu LSM (Gilliam and Pleim 2010; Xiu and Pleim, 2001). In addition, analysis nudging was used to continuously adjust the temperature, water vapor, and winds above the PBL toward the 6-h GFS analyses (e.g., Borge et al. 2008; Campbell et al. 2018; Harkey and Holloway 2013; Otte 2008a, b; Otte et al. 2012; Pleim and Gilliam 2009). Though additional procedures such as surface observation nudging and indirect soil moisture and soil temperature nudging (Pleim and Gilliam 2009; Pleim and Xiu 2003) are sometimes used to constrain the evolution of model simulations performed using the ACM2 scheme and Pleim-Xiu LSM, they are not employed during this study in order to maintain consistency with the other model simulations.

A second simulation was performed using the YSU PBL (Hong et al. 2006), Noah LSM (Chen and Dudhia, 2001; Ek et al. 2003), and Thompson microphysics (Thompson et al. 2008, 2016) schemes, which is hereafter referred to as the “YNT” configuration. Like the AP-XM simulation, this configuration employed the RRTMG longwave and shortwave radiation and Kain-Fritsch cumulus schemes on the outer two domains, along with grid nudging toward the GFS temperature, humidity, and wind analyses above the PBL. This particular set of schemes was chosen based on our previous studies showing that they performed well during the warm season across the United States (e.g., Harkey and Holloway 2013; Cintineo et al. 2014; Greenwald et al. 2016; Griffin et al. 2021; Henderson et al. 2021). Because there are dozens of parameterization schemes to choose from in the WRF model, we do not aim to find necessarily the best physics suite but instead to assess the potential of using other schemes to improve upon the performance of the baseline AP-XM configuration. The YSU PBL scheme is a first-order, non-local closure scheme that allows non-local mixing with explicit entrainment processes at the top of the PBL (Hong et al. 2006; Hong 2010). The Noah LSM is a community model that has been widely used within the weather and climate modeling communities (Campbell et al. 2019). It contains four soil layers (0-10, 10-40, 40-100, and 100-200 cm depth) along with vegetation canopy, soil drainage, and runoff models that allow it to simulate surface hydrological and radiative processes. A realistic representation of land surface processes becomes increasingly important when moving towards higher model resolutions (e.g., Sutton et al. 2006; Case et al. 2008).

The remaining six simulations (Table 1) use the YNT configuration as their baseline. These simulations are designed to assess the impact of three high-resolution surface datasets and analysis nudging above 2 km (rather than above the PBL) on the model accuracy when used individually or in combination. In particular, three simulations were run where the standard climatological or coarse-resolution surface datasets were replaced by high-resolution, real-time datasets depicting lake surface temperatures, green vegetation fraction (GVF), and soil moisture / soil temperature across the study region. These surface datasets and the methods used to incorporate them into the WRF model simulations are described in the next section. Simulations employing these datasets are referred to as “YNT_SST”, “YNT_GVF”, and “YNT_SOIL”, respectively. Another experiment was performed where analysis nudging was used above 2 km rather than above the PBL, which is referred to as the “YNT_N2KM” simulation. This change in nudging compared to the AP-XM and YNT baseline experiments was motivated by a modeling study by Odman et al. (2019) showing that the evolution of the nocturnal low-level jet across the Great Lakes region was more accurately simulated when nudging was withheld in the lower troposphere (e.g., below 2 km) when the PBL is shallow. Differences in the nocturnal low-level jet could affect the transport of ozone and its precursors from urban regions to Lake Michigan during the overnight hours. Finally, two “combination” simulations were performed where the 2-km analysis nudging approach was used along with all three of the high-resolution surface datasets (“YNT_SSSNG”) or only with the lake surface temperature and soil datasets (“YNT_SSN”). The latter simulation is included because it was found that this combination of surface datasets and analysis nudging generally led to the best results.

Table 1. List showing the parameterization schemes, model initialization datasets, surface datasets, and nudging approaches used during each of the eight WRF model experiments. Acronyms are described in the text.

	AP-XM	YNT	YNT_SST	YNT_GVF	YNT_SOIL	YNT_N2KM	YNT_SSSNG	YNT_SSN
PBL	ACM2	YSU	YSU	YSU	YSU	YSU	YSU	YSU
LSM	Pleim-Xiu	Noah	Noah	Noah	Noah	Noah	Noah	Noah

Deleted: local and non-local

Deleted: subgrid

Deleted: supergrid-scale

Deleted: Xu

Moved (insertion) [1]

Deleted: u

Moved up [1]: In addition, analysis nudging was used to continuously adjust the temperature, water vapor, and winds above the PBL toward the 6-h GFS analyses (e.g., Borge et al. 2008; Campbell et al. 2018; Harkey and Holloway 2013; Otte 2008a, b; Otte et al. 2012; Pleim and Gilliam 2009).

Deleted: Because this LSM only contains two layers (0-1 cm and 1-100 cm depth), indirect soil moisture and soil temperature nudging is used to improve the accuracy of these variables. The indirect nudging uses the weighted differences between simulated 2-m air temperature and relative humidity with available surface observations to reduce biases in the modeled soil moisture and soil temperature (Pleim and Gilliam 2009; Pleim and Xiu 2003). The 1-100 cm soil temperature was initialized as the average 2-meter temperature for the 10-day spin-up period (12-22 May 2017) using the IPXWRF utility (Pleim and Gilliam, 2009).

Deleted: Finally, hourly surface observations of temperature, humidity, winds, and sea level pressure from the Meteorological Assimilation Data Ingest System (MADIS, <https://madis.ncep.noaa.gov>) were used to perform surface nudging on all domains via the WRF OBSGRID utility.

Deleted: EPA

Deleted: EPA

Deleted: initialization

Deleted: initialization

Deleted: EPA

Deleted: initialization

Deleted: EPA

Deleted: Xu

Surface Layer	Pleim-Xiu	Monin-Obukhov	Monin-Obukhov	Monin-Obukhov	Monin-Obukhov	Monin-Obukhov	Monin-Obukhov	Monin-Obukhov	Monin-Obukhov
Micro.	Morrison	Thompson	Thompson	Thompson	Thompson	Thompson	Thompson	Thompson	Thompson
Cumulus	Kain-Fritsch	Kain-Fritsch	Kain-Fritsch	Kain-Fritsch	Kain-Fritsch	Kain-Fritsch	Kain-Fritsch	Kain-Fritsch	Kain-Fritsch
IC / BC	GFS-FNL	GFS-FNL	GFS-FNL	GFS-FNL	GFS-FNL	GFS-FNL	GFS-FNL	GFS-FNL	GFS-FNL
SST	<i>default</i>	<i>default</i>	GLSEA	<i>default</i>	<i>default</i>	<i>default</i>	GLSEA	GLSEA	<i>default</i>
GVF	<i>default</i>	<i>default</i>	<i>default</i>	VIIRS	<i>default</i>	<i>default</i>	VIIRS	<i>default</i>	<i>default</i>
Soil	<i>default</i>	<i>default</i>	<i>default</i>	<i>default</i>	SPoRT LIS	<i>default</i>	SPoRT LIS	SPoRT LIS	SPoRT LIS
Nudging	analysis above the PBL	analysis, above PBL	analysis, above PBL	analysis, above PBL	analysis, above PBL	analysis, above 2 km	analysis, above 2 km	analysis, above 2 km	analysis, above 2 km

Deleted: Xu

Deleted: L

Deleted: p

Deleted: p

Deleted: p

Deleted: *Initialized as 10-day ave. of 2-m temperature*

Formatted: Font: Italic

Deleted: ; obs nudging to MADIS

Deleted: initialization

Deleted: during

Deleted: persistent

Deleted: were

Deleted: then

24 2.2 Surface datasets

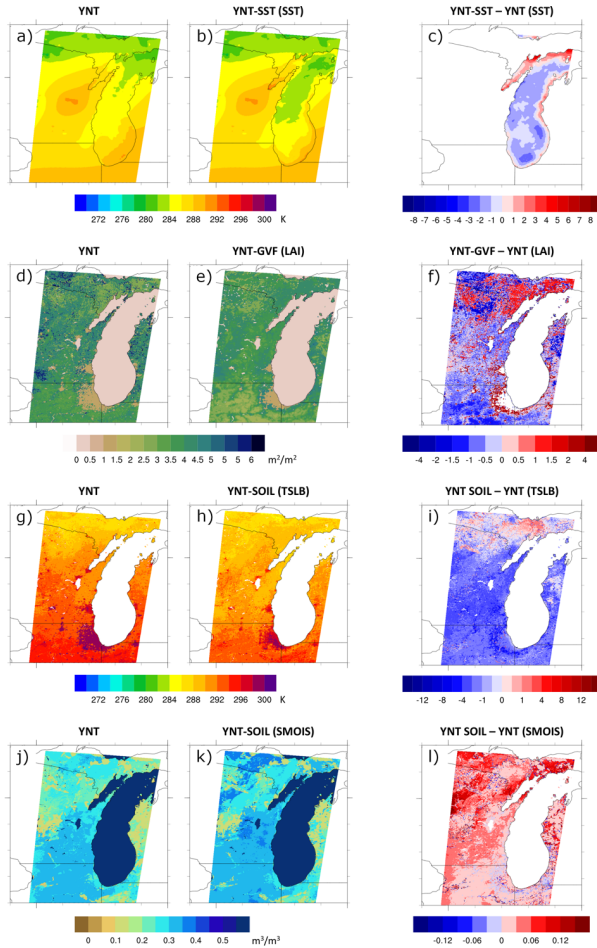
25 2.2.1 Lake surface temperatures

26 Daily maps of Great Lakes surface temperatures, with a horizontal resolution of ~1.3 km, were obtained from the Great Lakes
 27 Surface Environmental Analysis (GLSEA) produced at the NOAA Great Lakes Environmental Research Laboratory (Schwab
 28 *et al.* 1992). The lake surface temperatures are estimated using clear-sky infrared brightness temperatures from the Advanced
 29 Very High-Resolution Radiometer onboard multiple polar-orbiting satellites. If a surface retrieval is not possible *on* a given
 30 day due to cloud cover, a smoothing algorithm is applied to the previous analysis to maintain complete coverage. Only satellite
 31 observations are used to produce the daily lake surface temperature analyses, which Schwab *et al.* (1992) showed have small
 32 bias and root mean square error (1-1.5° C) when compared to buoys. The daily GLSEA analyses were used to overwrite the
 33 simulated surface temperatures for Great Lakes grid points at 00 UTC each day in the YNT_SST, YNT_SSN, and YNT_SSNG
 34 simulations using the WPS. Replacing the coarse-resolution (0.25°) GFS FNL surface temperatures (Fig. 2a) with the GLSEA
 35 analyses (Fig. 2b) led to warmer lake temperatures near the shoreline, especially along northern parts of Lake Michigan where
 36 temperatures were > 2 K warmer, and cooler temperatures across the rest of the lake, when averaged over the 22 May – 22
 37 June 2017 time period (Fig. 2c). This spatial pattern indicates that the finer horizontal resolution of the GLSEA dataset allows
 38 it to capture warmer temperatures in shallower waters near the shoreline while also depicting the cooler mid-lake temperatures
 39 due to the cooler-than-normal weather conditions that prevailed across the region in May (NCEI 2017).

40 2.2.2 VIIRS green vegetation fraction

41 GVF is the photosynthetically active fractional green vegetation cover within a grid cell, with higher values indicating more
 42 extensive actively transpiring vegetation. It is a key parameter in an LSM because vegetation representation is used to partition
 43 the incoming solar radiation into sensible, latent, and ground heat fluxes, where the latent heat flux is largely due to vegetation
 44 transpiration (e.g., Yin *et al.* 2016). Surface latent heat flux is sensitive to GVF because vegetation roots are able to access
 45 deeper soil moisture that would not otherwise be able to evaporate (Miller *et al.* 2006). For this study, we used daily global
 46 GVF derived using observations from the Visible Infrared Imaging Radiometer Suite (VIIRS; Vargas *et al.* 2015) in place of
 47 the default monthly climatology to constrain the evolution of vegetation in the YNT_GVF and YNT_SSNG simulations. The
 48 VIIRS GVF composite product is generated daily at 4-km resolution and available from the NOAA Comprehensive Large
 49 Array-data Stewardship System (CLASS). Ding and Zhu (2018) have shown that the VIIRS GVF product has smaller errors
 50 and bias than other satellite derived GVF datasets because of reduced atmospheric influences, improved observing capabilities
 51 in high biomass regions, better representation of vegetation canopies, and reduced bidirectional reflection distribution function
 52 effects. The real-time daily GVF analyses were used to overwrite the default monthly climatological vegetation fraction data

65 used by the WRF model at 00 UTC each day. Using real-time, satellite derived GVF in place of a monthly GVF climatology
66 has been shown to improve the representation of the surface energy budget and subsequent model forecasts during the warm
67 season (Case et al. 2014). In Fig. 2f, it is evident that use of the real-time GVF led to lower leaf area index (Fig. 2e; computed
68 internally by the WRF model) across most of the domain compared to the climatological vegetation data (Fig. 2d), with the
69 exception of some forested regions in the northern portion of the domain and bands of enhanced leaf area index surrounding
70 metropolitan areas such as Chicago. The lower leaf area index in agricultural areas is consistent with delayed crop growth due
71 to the cool spring weather, whereas the bands of higher leaf area index represent the impact of urban sprawl since the
72 climatological vegetation data shown in Fig. 2d was generated using satellite observations from the late 1980s and early 1990s
73 (see Gutman et al. 1995).
74



75

76

77

78

79

80

Figure 2. Average lake surface temperatures (K) from the (a) YNT and (b) YNT_SST simulations, with their differences shown in (c). Average leaf area index ($m^2 m^{-2}$) from the (d) YNT and (e) YNT_GVF simulations, with their differences shown in (f). Average 0-10 cm soil temperatures (K) from the (g) YNT and (h) YNT_SOIL simulations, with their differences shown in (i). Average 0-10 cm soil moisture content ($m^3 m^{-3}$) from the (j) YNT and (k) YNT_SOIL simulations, with their differences shown in (l). The averages for each variable were computed using data valid at 00 UTC each day during the 22 May – 22 June 2017 time period.

81 **2.2.3 SPoRT LIS soil moisture and temperature analyses**

82 A customized version of the Land Information System (LIS; Kumar et al. 2006) run at the Short-term Prediction Research and
83 Transition Center (SPoRT) was used to generate high-resolution soil moisture and soil temperature analyses. Version 3.6 of
84 the Noah LSM (Chen and Dudhia 2001) was run on a 1-km resolution domain covering the central and eastern United States
85 and nearby portions of southern Canada. Required inputs to run the Noah LSM were obtained from hourly analyses of surface
86 pressure, 2-m temperature, 2-m specific humidity, 10-m wind speed, and downwelling shortwave and longwave radiation from
87 the North American Land Data Assimilation System – Phase 2 (NLDAS-2; Xia et al. 2012). **No observations were assimilated**
88 **during the LIS runs.** Quantitative precipitation estimates (QPE) were obtained from the Multi-Radar Multi-Sensor (MRMS)
89 gauge-adjusted radar product (Zhang et al. 2016), the Global Data Assimilation System (GDAS; Wang et al. 2013), and
90 NLDAS-2. A simple blending methodology was used to incorporate the multiple sources of QPE because evaluation of the
91 real-time SPoRT-LIS product (Case 2016; Case and Zavodsky 2018; Blankenship et al. 2018) and preliminary LIS experiments
92 during this study revealed that the NLDAS-2 and MRMS precipitation products have a dry bias across the region. To reduce
93 this bias, the precipitation forcing used the average of the highest two values of the MRMS, GDAS, and NLDAS-2 QPE
94 datasets. Inspection of the blended precipitation product showed that the precipitation bias was reduced, while preserving
95 small-scale spatial details in the MRMS QPE product. Daily VIIRS GVF composites were also used to constrain vegetation
96 during the offline LIS-Noah simulation.
97

98 Following an initial spin-up of LIS using NLDAS-2 forcing data from 2012-2016 to remove memory of the prescribed initial
99 conditions, the final analysis from this run was used to restart the simulation on 01 January 2012 using NLDAS-2 atmospheric
00 forcing data, VIIRS GVF, and the merged QPE product. Soil moisture and soil temperature analyses from this LIS simulation
01 were then used to replace the corresponding variables in the YNT_SOIL, YNT_SSN, and YNT_SSN simulations at 00 UTC
02 each day from 12 May – 22 June 2017 **using the WPS.** Comparison of the 0-10 cm soil temperatures from the GFS (Fig. 2g)
03 and LIS (Fig. 2h), averaged over the 22 May – 22 June 2017 period, shows that the topsoil temperatures are noticeably cooler
04 in the LIS data across most of the region, except for northern parts of Wisconsin and Michigan. The cooler temperatures are
05 most prominent in suburban regions where the largest increases in GVF also occurred (Fig. 2f). For 0-10 cm soil moisture, the
06 LIS analyses are generally wetter across the domain (Fig. 2i), with the largest increases across forested regions of Wisconsin
07 and Michigan. Deeper soil layers exhibited similar differences between the GFS FNL and LIS datasets (not shown).

08 **2.3 Evaluation methods**

09 The accuracy of the WRF model simulations was assessed using hourly surface observations of temperature, humidity, and
10 winds from **the Meteorological Assimilation Data Ingest System (MADIS, <https://madis.ncep.noaa.gov/>)** during 22 May – 22
11 June 2017. **These observations were chosen because of their widespread availability and their important influence on surface**
12 **chemistry processes.** The model evaluations are performed on all three domains using observations from stations located on
13 the innermost domain surrounding Lake Michigan, which allows us to assess the behavior of each configuration as a function
14 of spatial resolution using the same set of stations. Version 1.4 of the Atmospheric Model Evaluation Tool (AMET; Appel et
15 al. 2011) from the EPA was used to collocate hourly observed and modeled values in a grid cell where a particular observation
16 station was located; and to calculate model performance statistics including bias and root mean square error.

17 **3. Results**

18 **3.1 Assessment of AP-XM and YNT baseline experiments**

19 This section contains a high-level assessment of the accuracy of the **AP-XM** and YNT baseline experiments on each domain,
20 with a more detailed evaluation of all experiments on the 1.3-km resolution domain provided in Section 3.2. Figure 3 shows
21 2-m temperature, 2-m water vapor mixing ratio, and 10-m wind speed errors for each domain computed using hourly surface
22 observations. The left column shows the bias for each variable and experiment, whereas the center and right columns show
23 the percentage changes in RMSE for each experiment relative to the **AP-XM** and YNT baseline experiments, respectively. A

Deleted: Direct insertion into the WRF model was possible because of the similarly configured Noah LSM used in both the LIS and WRF simulations.

Deleted: Analysis

Deleted: MADIS

Deleted: Note that these surface observations were also used to perform surface nudging during the EPA simulation, which will impact the results presented in Section 3 because surface nudging was not used during any of the YNT simulations.

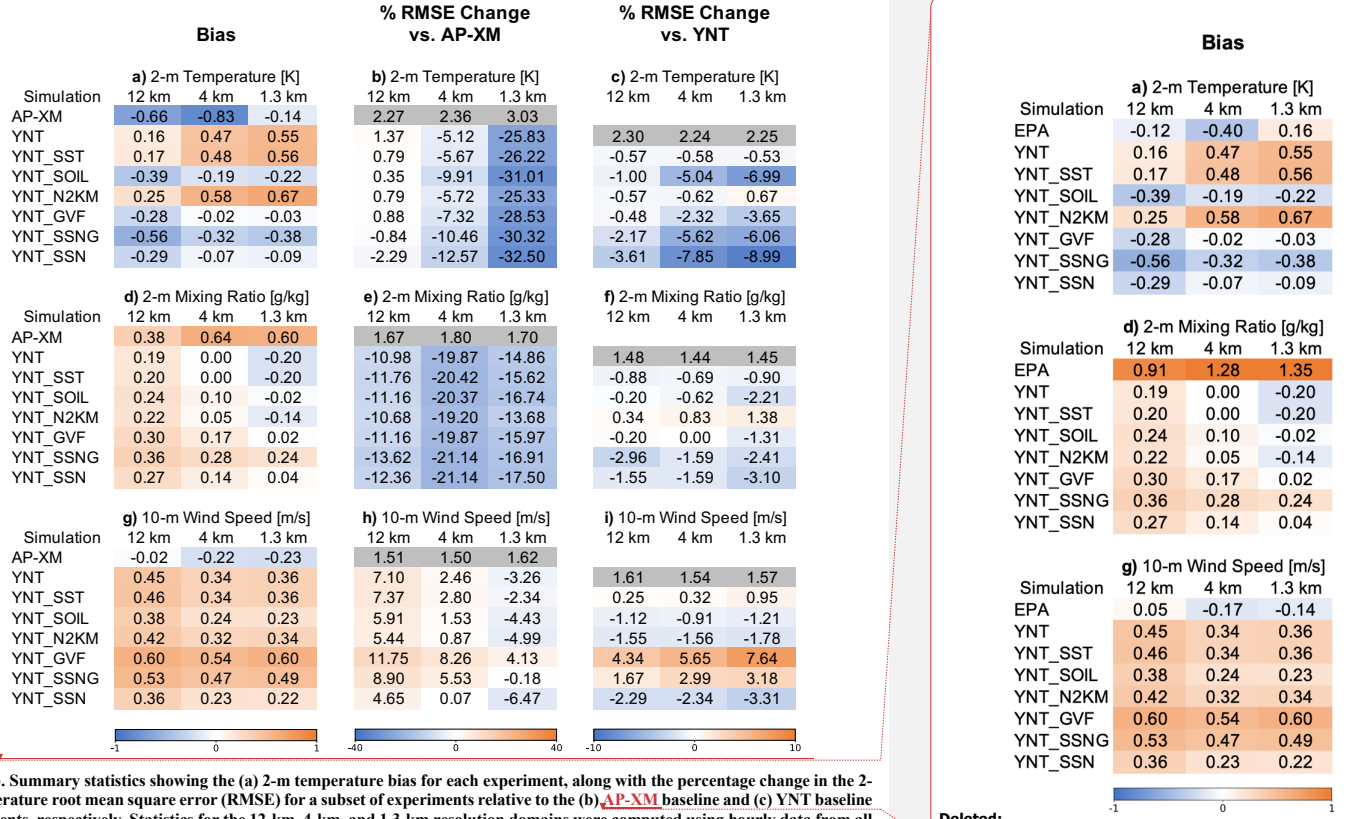
Deleted: EPA

Deleted: EPA

Deleted: EPA

36
37
38

negative (positive) value for a given variable and domain indicates that the RMSE for that experiment is smaller (larger) than the actual RMSE for the corresponding baseline experiment plotted in the gray box.



39

40 Figure 3. Summary statistics showing the (a) 2-m temperature bias for each experiment, along with the percentage change in the 2-
41 m temperature root mean square error (RMSE) for a subset of experiments relative to the (b) AP-XM baseline and (c) YNT baseline
42 experiments, respectively. Statistics for the 12-km, 4-km, and 1.3-km resolution domains were computed using hourly data from all
43 stations located on the 1.3-km resolution domain during 22 May – 22 June 2017. The actual RMSEs for the baseline experiments
44 (gray boxes) are also shown. Blue (orange) shading indicates a negative (positive) bias for a given experiment in (a), whereas blue
45 (orange) shading depicts smaller (larger) RMSE in a given experiment relative to the AP-XM and YNT baseline experiments in (b)
46 and (c). (d-f) Same as (a-c), except for showing statistics for 2-m mixing ratio. (g-i) Same as (a-c), except for showing statistics for
47 10-m wind speed.

48
49 Inspection of the YNT statistics reveals a consistent pattern in the RMSE where the percentage changes for each variable either
50 switch from positive to negative, or become more strongly negative, as the model resolution increases from 12 km to 1.3 km.
51 For temperature, the RMSE improves from being 1.37% larger than the AP-XM on the 12-km domain to 25.83% smaller on

Bias

Simulation	12 km	4 km	1.3 km
EPA	-0.12	-0.40	0.16
YNT	0.16	0.47	0.55
YNT_SST	0.17	0.48	0.56
YNT_SOIL	-0.39	-0.19	-0.22
YNT_N2KM	0.25	0.58	0.67
YNT_GVF	-0.28	-0.02	-0.03
YNT_SSNG	-0.56	-0.32	-0.38
YNT_SSN	-0.29	-0.07	-0.09

d) 2-m Mixing Ratio [g/kg]

Simulation	12 km	4 km	1.3 km
EPA	0.91	1.28	1.35
YNT	0.19	0.00	-0.20
YNT_SST	0.20	0.00	-0.20
YNT_SOIL	0.24	0.10	-0.02
YNT_N2KM	0.22	0.05	-0.14
YNT_GVF	0.30	0.17	0.02
YNT_SSNG	0.36	0.28	0.24
YNT_SSN	0.27	0.14	0.04

g) 10-m Wind Speed [m/s]

Simulation	12 km	4 km	1.3 km
EPA	0.05	-0.17	-0.14
YNT	0.45	0.34	0.36
YNT_SST	0.46	0.34	0.36
YNT_SOIL	0.38	0.24	0.23
YNT_N2KM	0.42	0.32	0.34
YNT_GVF	0.60	0.54	0.60
YNT_SSNG	0.53	0.47	0.49
YNT_SSN	0.36	0.23	0.22

Deleted: EPA
Deleted: EPA
Deleted: EPA
Deleted: 13.08
Deleted: EPA
Deleted: 18

58 the 1.3-km domain (Fig. 3b). A similar pattern is present for 10-m wind speed where the RMSE is 7.10% larger on the 12-km
59 domain, but then steadily decreases so that the RMSE becomes 3.26% smaller on the 1.3-km domain (Fig. 3h). The AP-XM
60 simulation had a smaller wind speed bias on all three domains compared to the YNT baseline. For 2-m mixing ratio (Fig. 3d,
61 3d), a positive bias on the 12-km domain increased at higher spatial resolutions for the AP-XM simulation but decreased and
62 turned into a negative bias for the YNT simulation, which also exhibits a large reduction in RMSE on all three domains. These
63 results indicate that the AP-XM physics suite becomes less accurate at higher resolutions and that the YNT configuration
64 provides superior performance on the 1.3-km domain when averaged across all stations. In the following sections, we will use
65 results from this domain to examine the impacts of the surface datasets and analysis nudging on the model accuracy with
66 respect to the AP-XM and YNT baseline experiments.

67 3.2 YNT sensitivity experiments

68 3.2.1 2-m temperature evaluation

69 To examine regional differences in model performance, Fig. 4 shows the 2-m temperature bias and RMSE computed separately
70 for each station using hourly observations from 22 May – 22 June 2017. For the AP-XM simulation, there is a north-south
71 gradient in the RMSE, with the largest errors across northern Illinois and Indiana (Fig. 4a). Stations near Lake Michigan have
72 the smallest RMSE due to its moderating influence on local weather conditions. Similar to the RMSE, the smallest biases
73 occurred in the northern part of the domain and along the eastern shoreline; however, biases along the western shoreline are
74 larger and of comparable magnitude to those at inland locations across Wisconsin and Illinois. Overall, the AP-XM simulation
75 had an RMSE of 3.03 K and a bias of -0.14 K when averaged across all stations (Figs. 3a-b). Switching to the YNT
76 parameterization suite greatly reduced the RMSE by 25.83% across the entire domain (Fig. 3b); however, the bias increased
77 to 0.55 K (Fig. 3a). The largest RMSE reductions (up to 45%) occurred in rural areas of northern Illinois, with similar RMSEs
78 found across the entire domain (Fig. 4b). The larger positive temperature bias in the YNT baseline simulation is primarily due
79 to larger errors in Wisconsin and within densely populated urban areas along the western Lake Michigan shoreline from
80 Chicago to Milwaukee (Fig. 4f). A mixed pattern of larger and smaller biases occurred elsewhere across the domain.

81
82 Inspection of the YNT sensitivity experiments shows that the smallest RMSEs occurred during the YNT_SOIL, YNT_SSN,
83 and YNT_SSSG simulations, with the average RMSE reduced by 30.32% to 32.5% relative to the EPA baseline (Fig. 3b) and
84 from 6.0% to 9.0% relative to the already greatly improved YNT baseline (Fig. 3c). On an individual basis, the high-resolution
85 soil dataset (YNT_SOIL) had the largest positive impact at most stations (Fig. 4d), whereas slightly larger RMSEs were
86 observed when using nudging (YNT_N2KM) (Fig. 4j). Comparison of the YNT_SSN and YNT_SSSG simulations (Fig. 4l,
87 4p) shows that inclusion of the VIIRS GVF dataset during the YNT_SSSG simulation led to slightly larger RMSE for stations
88 near the lakeshore, but similar or smaller errors for stations located further inland.

89
90 The bias pattern for the YNT simulations is more complex. Overall, the bias was largest (0.67 K) in the YNT_N2KM
91 simulation, with the smallest biases occurring in the YNT_GVF (-0.03 K) and YNT_SSN (-0.09 K) simulations (Fig. 3a).
92 Switching from the AP-XM to YNT baseline configurations led to larger biases across most of the domain, especially along
93 the southwestern shoreline of Lake Michigan (Fig. 4e-f). The high-resolution SST dataset had a minimal impact on the biases
94 (Fig. 4g) whereas they were smaller in the YNT_SOIL (Fig. 4h) and YNT_GVF (Fig. 4m) simulations relative to the YNT
95 baseline. Use of these two land datasets however led to much larger negative biases along the eastern shoreline of Lake
96 Michigan. When 2-km analysis nudging was used (YNT_N2KM), larger positive biases occurred from Chicago to Milwaukee,
97 with smaller biases along the eastern shoreline (Fig. 4n). The increased RMSE and bias near the western shoreline compared
98 to locations further inland during the YNT_N2KM simulation suggests that the modified nudging routine (applied to heights
99 above 2 km instead of above the PBL) may not work well for areas near Lake Michigan due to the moderating influence of
00 the lake on the PBL. Because the PBL tends to be more stable and shallower for locations over and near Lake Michigan due
01 to the cooler surface temperatures, this means that confining analysis nudging to above 2 km limits its ability to constrain the
02 evolution of the lower troposphere during the YNT_N2KM simulation. This behavior could also be due to deficiencies in the
03 YNT configuration over complex urban-lake transition zones.

Deleted: 6.26

Deleted: 32

Deleted: Though the EPA simulation has much larger bias and RMSE for 2-m mixing ratio on all domains (Fig. 3d, 3e), the same pattern emerges with this variable where it becomes less accurate at higher resolutions. Aside from using different parameterization schemes, the only difference between the baseline experiments is the use of soil and surface observation nudging in the EPA simulation.

Deleted: EPA

Deleted: , or the soil and surface nudging methods become less effective,...

Deleted: model

Deleted: . Because surface nudging is used on all domains during the EPA simulation, the poor performance on the 1.3-km domain suggests that it is no longer able to overcome deficiencies in the parameterization schemes, especially the Pleim-Xu LSM (see Section 3.3), at higher spatial resolutions. It is also possible that the lack of dense surface observations makes it challenging to effectively apply surface nudging at high resolutions since the observations lack sufficient spatial detail to capture small-scale atmospheric and land surface features. Regardless, Fig. 3 shows

Deleted: initialization

Deleted: both

Deleted: EPA

Deleted: analysis

Deleted: EPA

Deleted: generally

Deleted: EPA

Deleted: 0.16

Deleted: 18

Deleted: 29.7

Deleted: 31.9

Deleted: initialization

Deleted: initialization

Deleted: EPA

39 **3.2.2 2-m water vapor evaluation**

40 For the 2-m water vapor mixing ratio, switching to the YNT physics suite led to nearly a 15% reduction in the station-average
41 RMSE during the YNT simulation relative to the AP-XM baseline (Fig. 3e), with additional incremental reductions occurring
42 in all sensitivity experiments except for YNT_N2KM (Fig. 3f). The lower RMSE in all of the YNT simulations is primarily
43 due to the large reduction in bias (Fig. 3d). Whereas the AP-XM configuration had a large moist bias (0.60 g kg⁻¹), the YNT
44 bias was much smaller and also became negative (-0.20 g kg⁻¹). The bias was further reduced during most of the sensitivity
45 experiments, with only a slight increase during the YNT_SSN simulation. Overall, the YNT_SSN simulation had the smallest
46 RMSE and a bias close to zero when averaged across all of the stations.

47
48 Looking more closely at the individual stations (Fig. 5), it is evident that most of them have a positive (e.g., moist) bias when
49 the AP-XM configuration is used (Fig. 5e). The largest biases are located in the southern portion of the domain, especially for
50 stations near the lakeshore. In contrast, about two-thirds of the stations exhibit a negative bias during the YNT simulation (Fig.
51 5f). The spatial pattern of the biases is similar during all of the YNT sensitivity experiments; however, their magnitudes are
52 generally smaller, which is consistent with the overall statistics (Fig. 3d). For RMSE, the largest errors in the AP-XM
53 simulation occur primarily along the southern end of Lake Michigan, with generally smaller errors in the northern half of the
54 domain (Fig. 5a). The RMSE during the YNT simulation is smaller at most locations, especially along the shoreline, though a
55 few stations near the western shoreline have larger errors (Fig. 5b). Use of the SOIL and GVF datasets reduced the errors at
56 these nearshore locations (Fig. 5d, 5i), with the smallest errors at most stations occurring during the combination experiments
57 (YNT_SSN and YNT_SSN). As was the case with 2-m temperature, the most accurate 2-m water vapor analyses were
58 obtained during the YNT_SSN simulation.

59 **3.2.3 10-m wind speed evaluation**

60 Compared to the temperature and water vapor fields, changes to the 10-m wind speed statistics were much more modest during
61 the YNT simulations. Switching from the AP-XM configuration to the YNT configuration led to a 3.26% reduction in the
62 RMSE, but a larger bias that also changed sign from negative to positive (Fig. 3g). For the YNT experiments, the average
63 RMSE was slightly smaller during the YNT_SOIL and YNT_N2KM simulations (-1.21% and -1.78%, respectively), but
64 slightly larger (0.95%) during the YNT_SST simulation compared to the YNT baseline (Fig. 3i). Use of the GVF surface
65 dataset led to a 7.64% increase in the RMSE during the YNT_GVF simulation, primarily due to a larger wind speed bias.
66 Overall, the most accurate wind speed analyses were achieved during the YNT_SSN simulation, with an RMSE reduction of
67 6.47% across all stations.

68
69 Spatially, there is a latitudinal gradient in wind speed errors during the AP-XM simulation. The largest RMSEs are located
70 across the southern part of the domain (Fig. 6a), with mostly negative wind speed biases (up to 2 m s⁻¹) in the same region
71 transitioning to a mix of negative and positive biases in northern Wisconsin and Michigan (Fig. 6e). The RMSE and bias were
72 much smaller for stations around the southern shoreline of Lake Michigan during the YNT simulation; however, slightly larger
73 RMSEs are present across inland locations in the northern part of the domain (Fig. 6b). A similar spatial pattern of changes
74 relative to the AP-XM baseline occurred during the YNT sensitivity experiments, though the errors are generally larger during
75 the YNT_GVF simulation (Fig. 6i, 6m) and smaller during the YNT_SOIL (Fig. 6d, 6h) and YNT_N2KM (Fig. 6j, 6n)
76 simulations. The poor performance of the YNT_GVF and YNT_SSN simulations is primarily due to larger errors across
77 inland areas of Wisconsin where there are large positive wind speed biases (Fig. 6m, 6p), with similar errors elsewhere in the
78 domain.

Deleted: analysis

Deleted: 30

Deleted: EPA

Deleted: much

Deleted: notable

Deleted: EPA

Deleted: 1.35

Deleted: al

Deleted: all

Deleted: EPA

Deleted: is

Deleted: EPA

Deleted: initialization

Deleted: analysis

Deleted: EPA

Deleted: 32

Deleted: initialization

Deleted: 52

Deleted: EPA

Deleted: EPA

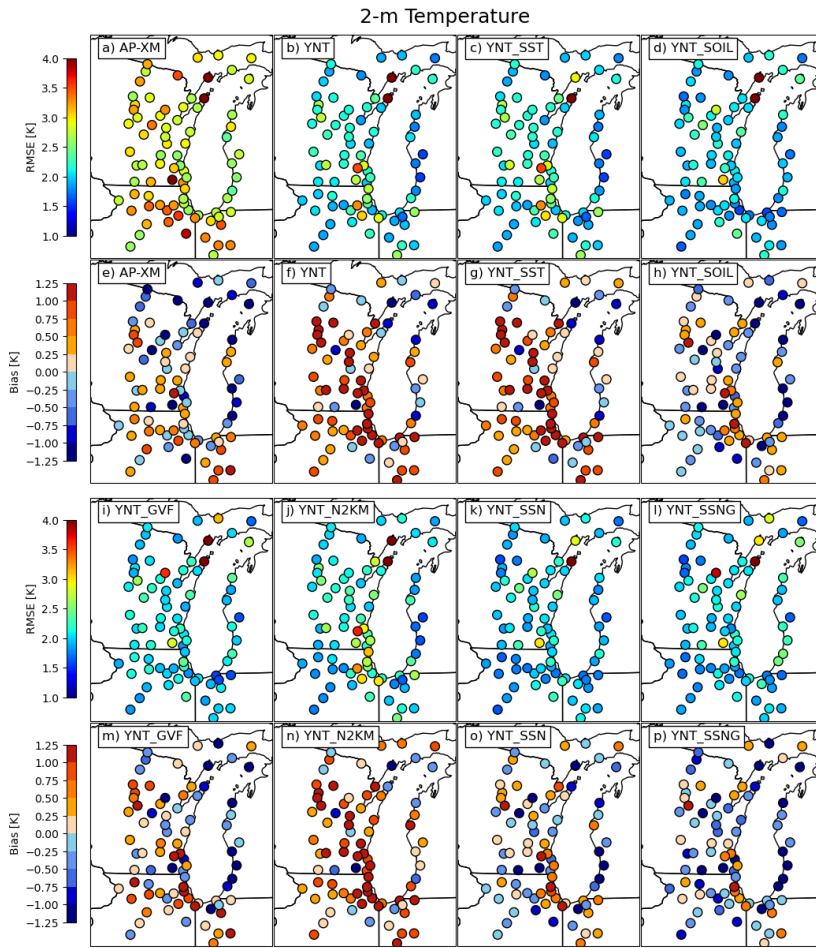
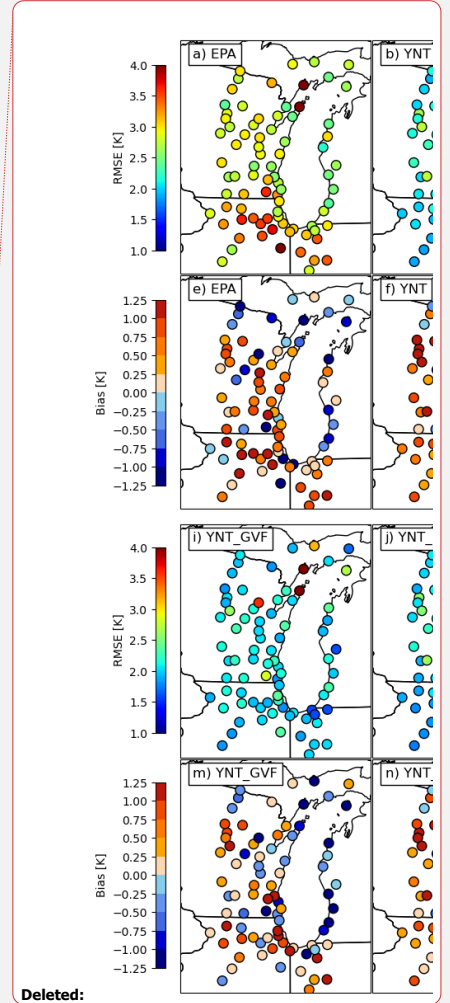
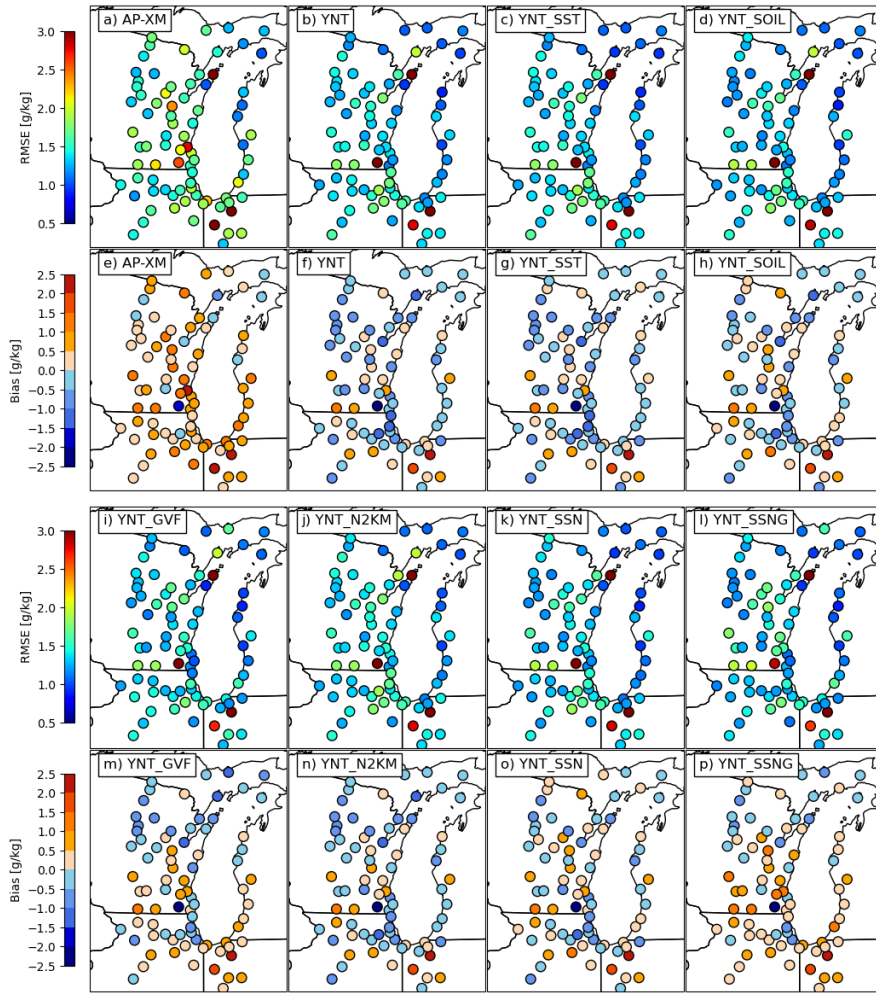


Figure 4. Maps showing the 2-m temperature (K) root mean square error (RMSE) and bias for each station on the 1.3-km domain computed using hourly data from 22 May – 22 June 2017. Statistics for the EPA, YNT, YNT_SST, and YNT_SOIL experiments are shown in (a)–(h), whereas results for the YNT_GVF, YNT_N2KM, YNT_SSN, and YNT_SSNG experiments are shown in (i)–(p).



99
00
01
02

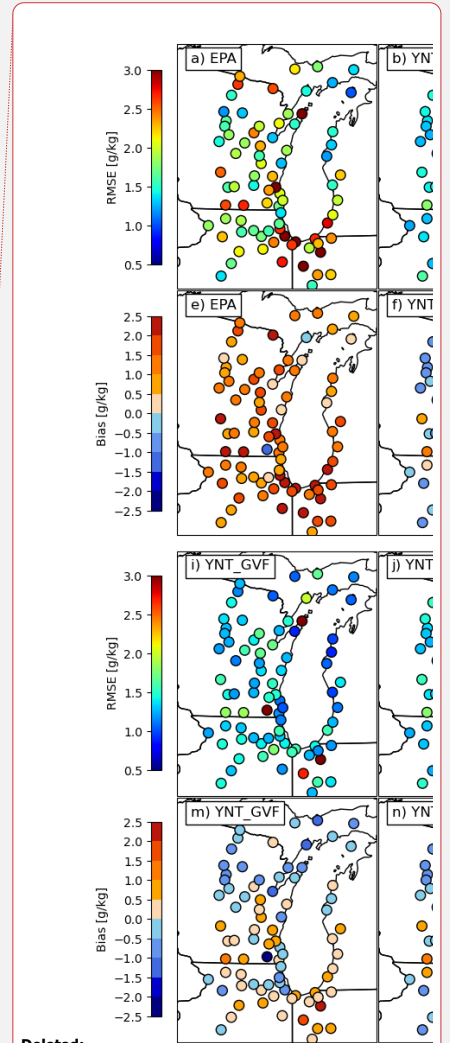
2-m Mixing Ratio



04

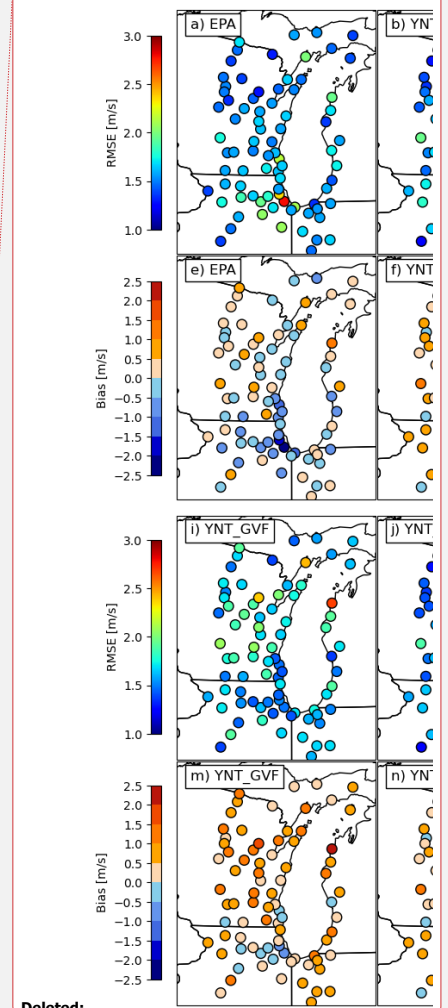
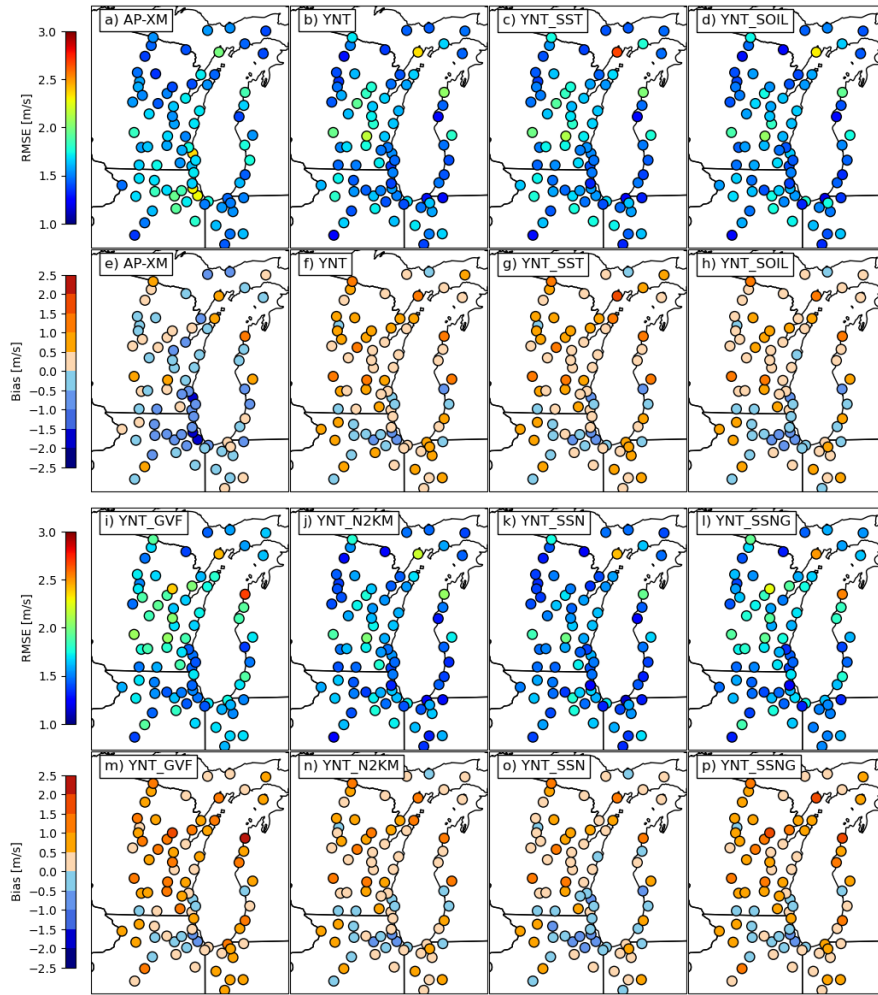
05

Figure 5. Same as Fig. 4, except for 2-m water vapor mixing ratio ($g\ kg^{-1}$).



Deleted:

10-m Wind Speed



Deleted:

07
08

Figure 6. Same as Fig. 4, except for 10-m wind speed ($m s^{-1}$).

10 3.2.4 Diurnal error characteristics

11 Fig. 7 shows the diurnal evolution of RMSE and bias for 2-m temperature, 2-m water vapor mixing ratio, and 10-m wind speed
12 at hourly intervals starting at 1900 local standard time (LST). The time series were computed by averaging over data from all
13 stations on the 1.3-km domain. Overall, it is apparent that the AP-XM simulation contains very different diurnal error patterns
14 than the YNT simulations. For example, the 2-m temperature bias exhibits a prominent diurnal cycle (Fig. 7b) characterized
15 by large positive/warm (negative/cool) biases during the night (day), resulting in an overall damping of the diurnal temperature
16 cycle. The warm biases exceed 2.0 K during most of the night (22–03 LST) and the cold biases are < -2 K for several hours
17 during the daytime (0900–1300 LST). These results indicate that the small temperature bias in the summary statistics for the
18 AP-XM simulation (Fig. 3a) is misleading because it obscures the presence of substantial biases of opposite signs during the
19 day and night. The RMSE is also much larger during the AP-XM simulation (Fig. 7a), with local maxima of 3.5 K at 1100 and
20 2300 LST, respectively, corresponding to peaks in the temperature biases. Switching to the YNT baseline greatly reduces the
21 temperature RMSE, and the bias time series is no longer characterized by the highly amplified diurnal pattern seen in the AP-
22 XM simulation. Examination of the YNT sensitivity experiments shows similar error patterns to the YNT baseline. The largest
23 differences occur at night when use of the GVF and SOIL datasets leads to smaller biases. In contrast, confining the analysis
24 nudging to above 2 km AGL (YNT_N2KM) slightly increases the RMSE and bias during the nighttime relative to the YNT
25 baseline.

27 For water vapor, the AP-XM simulation again exhibits larger bias and RMSE than the other simulations (Fig. 7c, 7d). It has a
28 large moist bias that ranges from 0.2 g kg⁻¹ shortly after sunrise to 0.9 g kg⁻¹ near 1900 LST, before decreasing to a relatively
29 stable bias of 0.6 g kg⁻¹ during the night. The RMSE is smaller in the YNT baseline simulation, with a dry bias evident for all
30 but the evening hours (1900–2200 LST). As is the case for temperature, the RMSE is smallest during the late-night hours and
31 then steadily increases during the day before reaching its maximum in the evening. All of the YNT sensitivity experiments
32 have similar RMSE and bias patterns to the YNT baseline, with the smallest (largest) spread between simulations occurring
33 during the nighttime (daytime) hours, possibly due to differences in the PBL depth and surface energy balance (see Fig. 8).
34 Comparison of the 10-m wind speed time series reveals that the AP-XM simulation has the smallest bias (~ 0.15 m s⁻¹) during
35 the night, but that the wind speeds are weaker than observed during the daytime, with the largest biases (-0.95 m s⁻¹) occurring
36 at noon (Fig. 7f). This diurnal pattern in the AP-XM simulation, characterized by winds that are too strong (weak) during the
37 night (day), stands in contrast to the mostly positive biases in the YNT simulations. The biases are tightly clustered in all of
38 the YNT experiments during the nighttime hours (2200–0700 LST), with the exception of the two simulations employing the
39 GVF dataset (YNT_GVF and YNT_SSNG) that are characterized by persistently larger positive biases. These two simulations
40 also have the largest RMSE (Fig. 7e). Further research is necessary to determine why incorporation of the high-resolution
41 GVF dataset leads to larger surface wind speed errors.

Deleted: EPA

Deleted: 5

Deleted: 3

Deleted: 5

Deleted: 10

Deleted: EPA

Deleted: EPA

Deleted: 4.4

Deleted: and 3.1 K

Deleted: 00

Deleted: 12

Deleted: EPA

Deleted: EPA

Deleted: much

Deleted: 9

Deleted: 1.7

Deleted: 1.3

Deleted: much

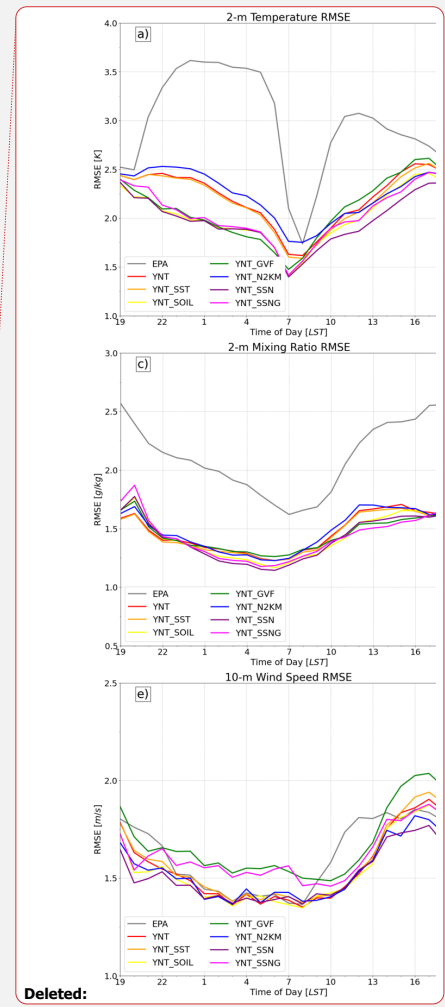
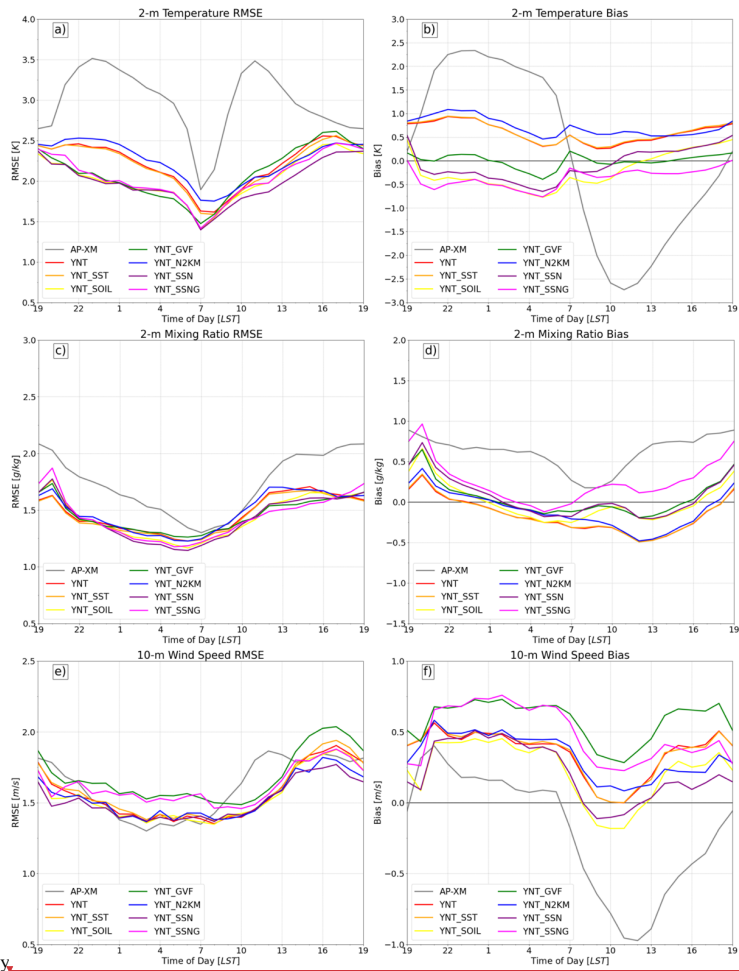
Deleted: EPA

Deleted: 3

Deleted: 8

Deleted: EPA

Deleted: initialization



66
 67
 68
 69
 70
 71

By **Figure 7.** Time series showing the diurnal evolution of (a-b) 2-m temperature (K) root mean square error (RMSE) and bias, (c-d) 2-m water vapor mixing ratio ($g\ kg^{-1}$) RMSE and bias, and (e-f) 10-m wind speed ($m\ s^{-1}$) RMSE and bias at hourly intervals starting at 1900 local standard time (LST). Errors were computed for each model simulation using observations from all stations located on the 1.3-km resolution domain during 22 May – 22 June 2017.

3.2.5 Surface Energy Budget Considerations

73 Near-surface atmospheric conditions can be strongly impacted by the partitioning of net surface radiation into sensible, latent,
74 and ground heat fluxes (Santanello et al. 2018). To examine this more closely, Fig. 8 shows time series depicting the average
75 diurnal evolution of the PBL height, net surface radiation, and sensible, latent, and ground heat fluxes during 22 May – 22
76 June 2017 computed using data from stations on the 1.3-km domain to maintain consistency with earlier results. Because in-
77 situ flux and PBL height observations are not available across the entire domain, the aim is not to examine the accuracy of the
78 simulated surface energy fluxes and PBL height, but rather to use these variables to help explain differences in the near-surface
79 temperature, water vapor, and wind speed errors in the model simulations. All of the variables were obtained directly from the
80 WRF output files. The net surface radiation is defined as the sum of the upward and downward shortwave and longwave
81 radiation fluxes at the surface.

83 Inspection of Fig. 8 reveals large differences between the AP-XM and YNT simulations. The PBL is ~50-150 m deeper in the
84 AP-XM simulation during the nighttime but then becomes much shallower than the YNT simulations from mid-morning
85 through the afternoon (1000–1600 LST) with the daytime maximum in PBL height occurring ~2 h later (Fig. 8a). The AP-XM
86 simulation is also characterized by a smoother and less amplified diurnal evolution. For the YNT simulations, the PBL heights
87 are tightly clustered during the night (2100 – 0700 LST) but begin to diverge during the morning and reach their largest
88 differences during the afternoon. In particular, simulations employing the high-resolution soil moisture analyses (YNT_SOIL,
89 YNT_SSN, and YNT_SSN) have average PBL heights that are ~100 m lower than the other YNT simulations. These three
90 simulations also have slightly lower sensible heat flux (Fig. 8c) and higher latent heat flux during the afternoon (Fig. 8d),
91 which is consistent with the wetter and cooler topsoil layer in the SPoRT LIS analyses (Fig. 2g-l) and cooler 2-m temperatures
92 (Figs. 3a, 7b). Using the SST and GVF datasets and confining analysis nudging to above 2 km had minimal impact on the PBL
93 heights in the YNT_SST, YNT_GVF, and YNT_N2KM simulations; however, sensible and latent heat fluxes are slightly
94 smaller during the afternoon in the YNT_GVF simulation.

96 Comparison of the AP-XM and YNT simulations also reveals large differences in the surface energy flux time series. For
97 example, the AP-XM simulation has much smaller sensible heat flux during the daytime (Fig. 8c) and the latent heat flux
98 remains relatively large during the night (Fig. 8d). Though the AP-XM and YNT simulations produce similar magnitudes of
99 latent heat flux during the day, the afternoon maximum is delayed by 2 h in the AP-XM simulation. The combination of a
100 shallower PBL during the day (Fig. 8a) and higher latent heat flux at night likely contributes to the persistent large moist bias
101 in the 10-m water vapor mixing ratio (Figs. 3d, 7d) during the AP-XM simulation. Another noteworthy feature of the AP-XM
102 simulation is that the ground heat flux remains negative at all times. This unphysical behavior stands in sharp contrast to the
103 more realistic evolution during the YNT simulations where the positive (negative) ground heat flux during the night (day)
104 indicates that heat is being transferred from (toward) the ground toward (from) the atmosphere due to cooler (warmer) surface
105 temperatures. These results indicate that the poor performance of the AP-XM simulation on the 1.3-km domain when assessed
106 using near-surface moisture, temperature, and wind observations is likely due to the presence of vastly different and sometimes
107 unphysical surface energy fluxes.

109 The lower accuracy of the AP-XM simulation could be due to limitations in the parameterization schemes when used at higher
110 spatial resolution. This possibility is supported by Fig. 9, which shows the evolution of the PBL height and surface fluxes on
111 the 12-km domain computed using simulated data from all stations on the 1.3-km domain. Differences between the AP-XM
112 and YNT simulations are much smaller both in timing and magnitude on the 12-km domain. For example, the time series for
113 PBL height, sensible heat flux, and latent heat flux are very similar for all of the simulations. Though the ground heat flux
114 time series for the AP-XM simulation continues to be an outlier at this resolution, it now has the correct diurnal cycle with
115 positive (negative) values during the night (day). The improved simulation of surface fluxes on the 12-km domain likely
116 contributes to the more accurate temperature and wind speed analyses in the AP-XM simulation at that resolution (Fig. 3a-b,
117 3g-h). The presence of persistently higher latent heat flux (Fig. 9d) leads to a positive moisture bias in the AP-XM simulation
118 (Fig. 3d-e); however, the bias is smaller on the 12-km domain than it was on the 1.3-km domain. Inspection of the surface
119 energy fluxes and PBL height on the 4-km domain revealed larger differences between the AP-XM and YNT simulations (not
120 shown), but not as large as those on the 1.3-km domain. Though it is not the focus of this research, differences in PBL height
121 between the AP-XM and YNT simulations could be due to differences in vertical mixing strength and entrainment flux in the

Deleted: ¶

Deleted: sensible, latent, and ground heat fluxes

Deleted: EPA

Deleted: 10

Deleted: 20

Deleted: EPA

Deleted: 1-

Deleted: EPA

Deleted: EPA

Deleted: EPA

Deleted: EPA

Deleted: EPA

Deleted: EPA

Deleted: EPA

Deleted: EPA

Deleted: EPA

Deleted: on the 1.3-km domain

Deleted: the use of soil nudging in the Pleim-Xu LSM because the observations used in the nudging approach are typically too coarse to provide the fine-scale geographically induced details needed to perform high-quality soil nudging (J. Pleim, personal comm....

Deleted:)

Deleted: EPA

Deleted: EPA

Deleted: EPA

Deleted: EPA

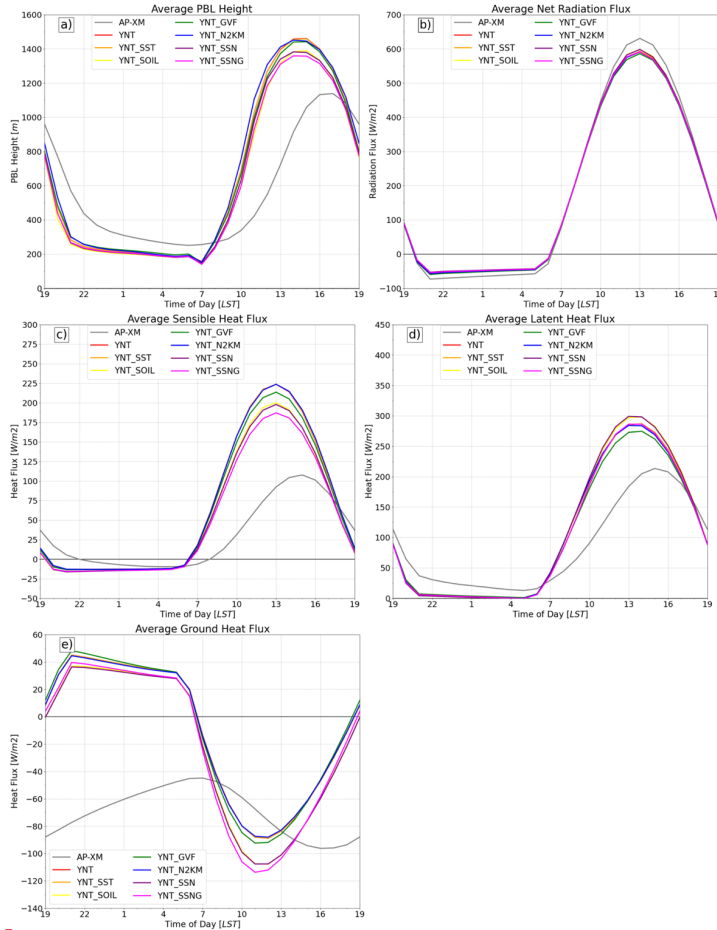
Deleted: each of

Deleted: EPA

51
52
53

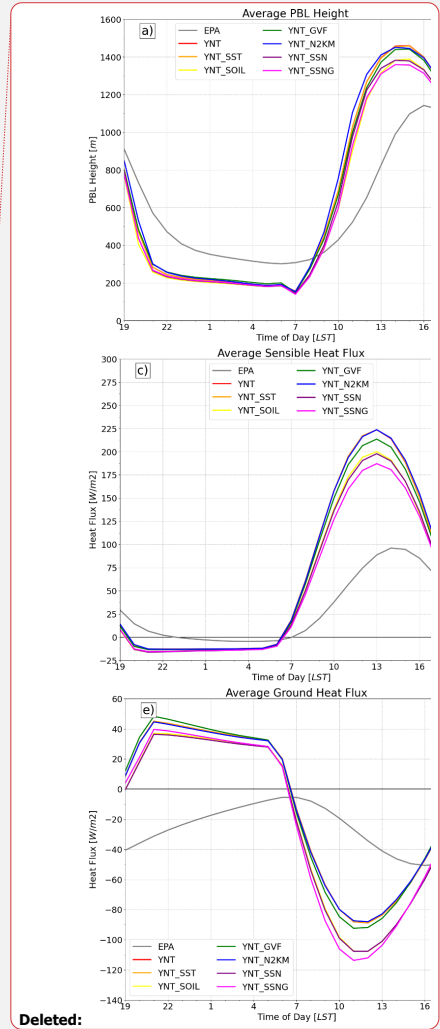
AMC2 and YSU PBL schemes (e.g., Hu et al. 2010). Together, these results show that the AP-XM simulation performs well at 12-km resolution, but that its accuracy decreases with increasing model resolution.

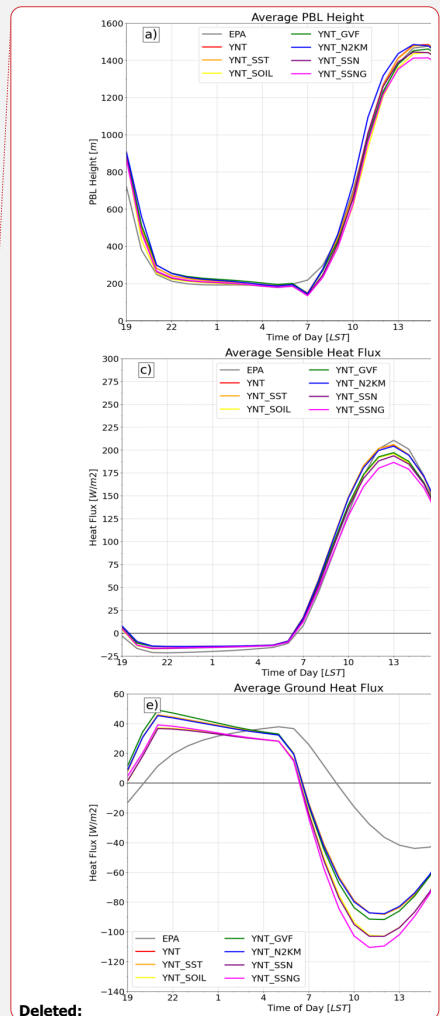
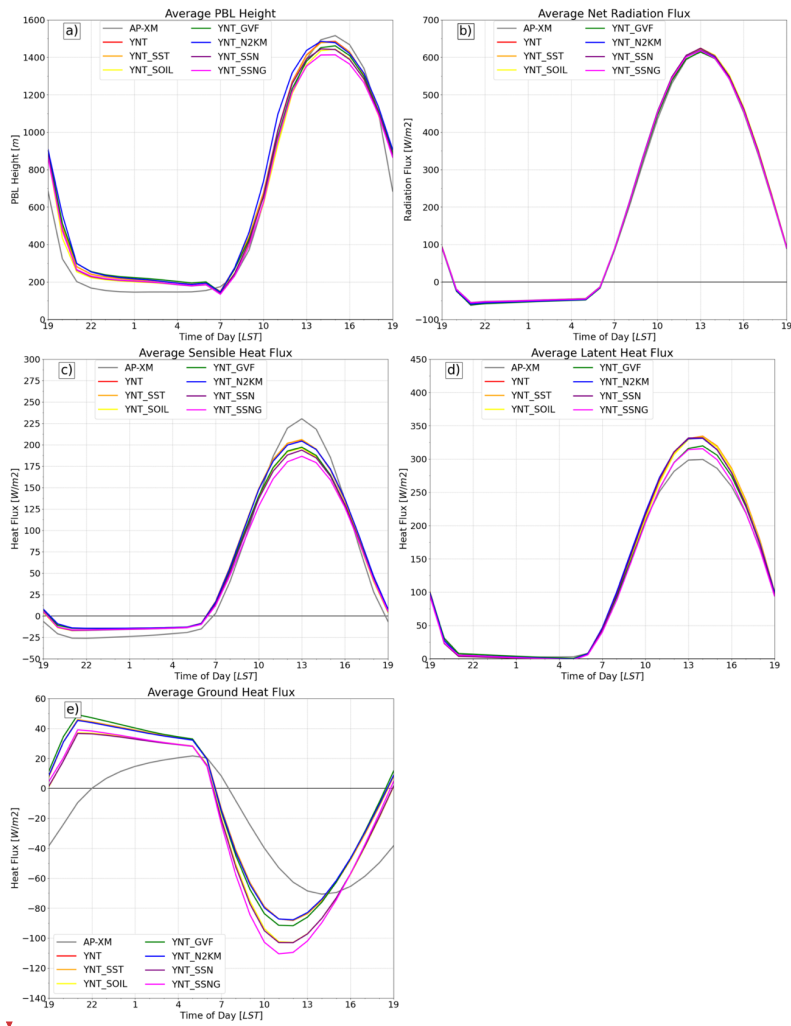
Deleted: EPA



54
55
56
57
58

Figure 8. Time series showing the diurnal evolution of the (a) planetary boundary layer height (m), (b) net radiation ($W m^{-2}$), (c) sensible heat flux ($W m^{-2}$), (d) latent heat flux ($W m^{-2}$), and (e) ground heat flux ($W m^{-2}$) at hourly intervals starting at 1900 local standard time (LST), averaged over all stations on the 1.3-km domain during 22 May – 22 June 2017. Results are shown individually for each of the model simulations.





Deleted:

Deleted:

61

62

63

Figure 9. Same as Fig. 8, except for showing results on the 12-km domain. Time series were computed using simulated data from all stations located on the 1.3-km domain.

66 4. Discussion and conclusions

67 In this study, eight WRF model simulations were performed to assess the impact of different parameterization schemes, surface
68 datasets, and analysis nudging on the simulation of surface energy fluxes and near-surface atmospheric conditions in the Lake
69 Michigan region during a 1-month period (22 May – 22 June 2017) corresponding to the LMOS field campaign. The
70 simulations employed a triple-nested domain configuration containing 12-, 4-, and 1.3-km resolution grids, respectively. Two
71 baseline simulations (AP-XM and YNT) employing different sets of parameterization schemes were performed to assess the
72 importance of different physics suites. The YNT configuration additionally served as the baseline for six sensitivity simulations
73 that were used to assess the impact of three satellite- and model-derived surface datasets and analysis nudging. Simulations
74 were run where standard climatological or coarse-resolution surface datasets were replaced by high-resolution, real-time
75 datasets depicting lake surface temperatures, GVF, and soil moisture/soil temperature. Near-surface temperature, water vapor,
76 and wind observations were used to assess the accuracy of each model simulation.

77
78 The AP-XM configuration generally produced more accurate near-surface analyses on the 12-km domain, with the exception
79 of a moist bias in the 2-m water vapor mixing ratio, but its relative performance decreased with finer model grid resolution.
80 Evaluation of the AP-XM simulation showed that the diurnal evolution of the sensible and latent heat fluxes was similar to the
81 YNT simulation on the 12-km domain but differed greatly on the 1.3-km nested domain where it had much smaller sensible
82 heat flux during the daytime and larger latent heat flux at night. The increased latent heat flux combined with a shallower PBL
83 contributed to the large moist bias in the 2-m water vapor mixing ratio. The evolution of the AP-XM ground heat flux was
84 physically unrealistic on the 1.3-km domain because it remained negative at all times rather than changing signs between day
85 and night as occurred during the YNT simulations. Because the evolution of the surface energy fluxes was more realistic on
86 the 12-km domain, the poorer performance on the 4- and 1.3-km domains suggests that the Pleim-Xiu LSM is unable to
87 adequately represent surface fluxes at higher resolutions. This could be due to its use of two soil layers including a very shallow
88 (1 cm) topsoil layer that make it difficult to fully represent fine-scale features and soil heat fluxes. Increasing the number of
89 soil layers in the Pleim-Xiu LSM could potentially improve its ability to simulate energy fluxes on high-resolution domains.
90 In addition, use of observation nudging and soil moisture and soil temperature nudging as used in Torres-Vazquez et al. (2022)
91 would also help constrain the evolution of this simulation. Though these specialized nudging techniques were not employed
92 in our study due to their added complexity and confounding influence on the model evaluations because the same observations
93 used in the nudging procedure would also be used to assess the accuracy of the simulations, their utility could be assessed in
94 future work.

95
96 Inspection of the YNT statistics revealed a pattern where the percentage change in the RMSEs for 2-m temperature, 2-m water
97 vapor mixing ratio, and 10-m wind speed relative to the AP-XM baseline improved as the model resolution increased from 12
98 km to 1.3 km. Switching to the YNT configuration led to substantial decreases in RMSE for 2-m temperature (25.8%) and 2-
99 m water vapor mixing ratio (14.9%), and a more modest 3.3% reduction in the RMSE for 10-m wind speed, when assessed
00 using all stations on the 1.3-km domain. Despite the already large error reductions when using the YNT parameterization suite,
01 additional improvements occurred in most variables when the high-resolution surface datasets were incorporated into the
02 modeling platform. Evaluation of the YNT sensitivity experiments showed that the high-resolution soil dataset had the largest
03 positive impact on temperature and water vapor errors and the second largest impact on wind speed. Use of the GVF and SST
04 datasets also led to more accurate temperature and water vapor simulations, but some degradations in the wind speed,
05 especially when using the GVF dataset. Only the simulation employing analysis nudging above 2 km produced more accurate
06 10-m wind speed analyses; however, 2-m temperature errors were larger along the western shoreline of Lake Michigan when
07 the nudging was confined to levels above 2 km instead of above the PBL. This suggests that the modified nudging approach
08 may not work well for areas near Lake Michigan where the PBL tends to be shallower because it reduces its ability to constrain
09 the evolution of the lower troposphere. Despite this limitation, the most accurate near-surface simulations were obtained during
10 the experiment that employed analysis nudging above 2 km combined with the high-resolution SST and soil datasets. Slight
11 degradation occurred when the satellite GVF dataset was included.

12
13 With these differences in near-surface temperature, humidity, and winds across model configurations and inputs, we can expect
14 ensuing differences in the accuracy of model simulations of the production and transport of ozone precursors, as well as the

- Deleted: initialization
- Deleted: The "EPA"
- Deleted: ed
- Deleted: parameterization schemes and a model configuration similar to that used at the EPA, including soil and surface observation nudging. A second simulation ("YNT") was performed using different parameterization schemes
- Deleted: that are easier to use because they do not require soil and surface observation nudging
- Deleted: Another important difference is that the YNT simulation used the more sophisticated Noah LSM to simulate land processes rather than the Pleim-Xu LSM that was used in the EPA simulation.
- Deleted: then
- Deleted: to perform
- Deleted: additional
- Deleted: initialization
- Deleted: initialization
- Deleted: EPA
- Deleted: large
- Deleted: accuracy greatly
- Deleted: The superior performance of the EPA simulation on the 12-km domain is partially an artifact of its use of surface observation nudging because the same observations used in the nudging routine were also used for verification. However, surface observation nudging was also used on the 4-km and 1.3-km domains in the EPA simulation, which indicates that it becomes less effective at constraining the evolution of the atmosphere at higher spatial resolutions. This is possible because the surface observations lack sufficient spatial density to accurately capture and constrain small-scale features associated with abrupt changes in land surface characteristics such as occurs along coastlines or the interface between urban and rural areas.
- Deleted: EPA
- Deleted: EPA
- Deleted: Xu
- Deleted: Xu
- Deleted: and reduce its dependence on nudging to constrain its evolution
- Deleted: consistent
- Deleted: EPA
- Deleted: The superior performance at higher resolutions when using the YNT configuration was achieved without using soil nudging or surface observation nudging.
- Deleted: 30
- Deleted: of the
- Deleted: initialization
- Deleted: initialization

63 production of ozone. In part II of this study (Pierce et al. 2023), we evaluate these impacts on ozone forecasts in the Lake
64 Michigan region using meteorological analyses obtained from the baseline AP-XM and optimized WRF model configurations
65 as input to CMAQ model simulations.

Deleted: EPA

Deleted: are used

Deleted: to assess their impact on ozone forecasts in the Lake Michigan region

66 Data availability

67
68
69 All raw data can be provided by the corresponding authors upon request.

70 Author contributions

71
72
73 JAO and RBP planned the study; MH performed the model simulations; JLC provided surface datasets; JAO, LMC, RBP, and
74 MH analyzed the data; JAO wrote the manuscript; JAO, LMC, JLC, RBP, MH, AL, DSH, ZA, TN, and CRH reviewed and
75 edited the manuscript.

Formatted: Font: (Default) Times New Roman, 10 pt

76 Competing interests

77
78
79 The authors declare that they have no conflicts of interest.

80 Acknowledgments

81
82
83 Funding for this project was provided by the NASA Health and Air Quality (HAQ) program via grant #80NSSC18K1593.

84 References

85 Adelman, Z.: LADCO public issues, <https://www.ladco.org/public-issues/>, 2020.

86
87 Appel, K.W., Gilliam, R. C., Davis, N., Zubrow, A., and Howard, S. C.: Overview of the atmospheric model evaluation tool
88 (amet) v1.1 for evaluating meteorological and air quality models, Environ. Model. Softw., 26, 434-443, 2011.

89
90 Berg, A., and Coauthors, 2014. Impact of soil moisture–atmosphere interactions on surface temperature distribution, J.
91 Climate, 27, 7976–7993. <https://doi.org/10.1175/JCLI-D-13-00591.1>, 2014.

92
93 Blankenship, C. B., Case, J. L., Crosson, W. L., and Zavodsky, B. T.: Correction of forcing-related artifacts in a land surface
94 model by satellite soil moisture data assimilation, IEEE Geosci. Remote Sens. Lett., 15, 498-502,
95 doi:10.1109/LGRS.2018.2805259, 2018.

96
97 Bloomer, B. J., Stehr, J. W., Piety, C. A., Salawitch, R. J., and Dickerson, R. R.: Observed relationships of ozone air pollution
98 with temperature and emissions, Geophys. Res. Lett., 36, L09803, doi:10.1029/2009GL037308, 2009.

99
100 Borge, R., Alexandrov, V., del Vas, J. J., Lumbreras, J., and Rodriguez, E.: A comprehensive sensitivity analysis of the WRF
101 model for air quality applications over the Iberian Peninsula, Atmos. Environ., 42, 8560-8574, doi:
102 10.1016/j.atmosenv.2008.08.032, 2008.

103
104 Camalier, L., Cox, W., and Dolwick, P.: The effects of meteorology on ozone in urban areas and their use in assessing ozone
105 trends, Atmos. Environ., 41, 7127-7137, 2007.

106
107 Campbell, P. C., Bash, J. O., and Spero, T. L.: Updates to the Noah land surface model in WRF-CMAQ to improve simulated
108 meteorology, air quality, and deposition. Journal of Advances in Modeling Earth Systems, 11, 231– 256.
109 <https://doi.org/10.1029/2018MS001422>, 2019.

- 14
15 Case, J. L.: From drought to flooding in less than a week over South Carolina, *Results Phys.*, 6, 1183–1184,
16 doi:10.1016/j.rinp.2016.11.012, 2016.
17
18 Case, J. L., Crosson, W. L., Kumar, S. V., Lapenta, W. M., and Peters-Lidard, C. D.: Impacts of High-Resolution Land Surface
19 Initialization on Regional Sensible Weather Forecasts from the WRF Model, *J. Hydrometeor.*, 9, 1249-1266, 2008.
20
21 Case, J. L. and Zavadsky, B. T.: Evolution of 2016 drought in the southeastern United States from a land surface modeling
22 perspective, *Results Phys.*, 8, 654–656, doi:10.1016/j.rinp.2017.12.029, 2018.
23
24 Chen, F., and Dudhia, J.: Coupling an advanced land-surface/hydrology model with the Penn State/NCAR MM5 modeling
25 system. Part I: Model description and implementation, *Mon. Wea. Rev.*, 129, 569-585, 2001.
26
27 Cintineo, R., Otkin, J. A., Kong, F., and Xue, M.: Evaluating the accuracy of planetary boundary layer and cloud microphysical
28 parameterization schemes in a convection-permitting ensemble using synthetic GOES-13 satellite observations, *Mon. Wea.*
29 *Rev.*, 142, 163-182, 2014.
30
31 Cleary, P. A., and Coauthors: Ozone distributions over southern Lake Michigan: Comparisons between ferry-based
32 observations, shoreline-based DOAS observations and model forecasts. *Atmos. Chem. Phys.*, 15, 5109–5122, <https://doi.org/10.5194/acp-15-5109-2015>, 2015.
33
34 [Coates, J., Mar, K. A., Ojha, N., and Butler, T. M.: The influence of temperature on ozone production under varying NOx conditions – a modelling study, *Atmos. Chem. Phys.*, 16, 11601–11615, <https://doi.org/10.5194/acp-16-11601-2016>, 2016.](https://doi.org/10.5194/acp-16-11601-2016)
35
36 [Dawson, J. P., Adams, P. J., and Pandis, S. N.: Sensitivity of ozone to summertime climate in the eastern USA: A modeling case study, *Atmos. Environ.*, 41, 1494-1511, 2007.](https://doi.org/10.1016/j.atmosenv.2007.04.011)
37
38 [Ding, H., and Zhu, Y.: GVF Algorithm Theoretical Basis Document, NDR Vegetation Products System Algorithm Theoretical Basis Document, NOAA/NESDIS, 62 pp. \[https://www.ospo.noaa.gov/Products/documents/GVF_ATBD_V4.0.pdf\]\(https://www.ospo.noaa.gov/Products/documents/GVF_ATBD_V4.0.pdf\), 2018.](https://www.ospo.noaa.gov/Products/documents/GVF_ATBD_V4.0.pdf)
39
40
41 Dirmeyer, P.A., and Halder, S., 2016. Sensitivity of numerical weather forecasts to initial soil moisture variations in CFSv2.
42 *Weather Forecast.* 31 (6), 1973–1983. <https://doi.org/10.1175/WAF-D-16-0049.1>, 2016.
43
44 Dye, T. S., Roberts, P. T. and Korc, M. E.: Observations of transport processes for ozone and ozone precursors during the
45 1991 Lake Michigan Ozone Study. *J. Appl. Meteor.*, 34, 1877–1889, [https://doi.org/10.1175/1520-0450\(1995\)034<1877:OO](https://doi.org/10.1175/1520-0450(1995)034<1877:OO)
46 [TPFO>2.0.CO;2](https://doi.org/10.1175/1520-0450(1995)034<1877:OOTPFO>2.0.CO;2), 1995.
47
48 Ek, M. B., and Coauthors: Implementation of Noah land surface model advances in the National Centers for Environmental
49 Prediction operational mesoscale Eta model, *J. Geophys. Res.*, 108, 8851, doi:10.1029/2002JD003296, 2003.
50
51 Foley, T., Betterton, E. A., Robert Jacko, P. E., and Hillery, J.: Lake Michigan air quality: The 1994–2003 LADCO Aircraft
52 Project (LAP). *Atmos. Environ.*, 45, 3192–3202, <https://doi.org/10.1016/j.atmosenv.2011.02.033>, 2011.
53
54 Gilliam, R. C., and Pleim, J. E.: Performance assessment of new land surface and planetary boundary layer physics in the
55 WRF-ARW, *J. Appl. Meteorol. Climatol.*, 49, 760-774, doi: [10.1175/2009JAMC2126.1](https://doi.org/10.1175/2009JAMC2126.1), 2010.
56
57 Greenwald, T. J., Pierce, R. B., Schaack, T., Otkin, J. A., Rogal, M., Bah, K. and Huang, H.-L.: Near real-time production of
58 simulated GOES-R Advanced Baseline Imager data for user readiness and product validation, *Bull. Am. Meteorol. Soc.*, 97,
59 245-261, 2016.
60
61 Griffin, S. M., and Coauthors: Evaluating the impact of planetary boundary layer, land surface model, and microphysics
62 parameterization schemes on upper-level cloud objects in simulated GOES-16 brightness temperatures. *J. Geophys. Res. - Atmos.*, 126, e2021JD034709. <https://doi.org/10.1029/2021JD034709>, 2021.
63
64
65
66

67
68 Gutman, G., Tarpley, D., Ignatov, A., and Olson, S.: The enhanced NOAA global land data set from the Advanced Very High
69 Resolution Radiometer. *Bull. Am. Meteor. Soc.*, 76, 1141–1156, 1995.
70
71 Harkey, M., and Holloway, T.: Constrained dynamical downscaling for assessment of climate impacts, *J. Geophys. Res.*
72 *Atmos.*, 118, 2316–2148, doi: 10.1002/jgrd.50223, 2013.
73
74 Henderson, D. S., Otkin, J. A., and Mecikalski, J. R.: Evaluating convective initiation in high-resolution numerical weather
75 prediction models using GOES-16 infrared brightness temperatures, *Mon. Wea. Rev.*, 149, 1153–1172, 2021.
76
77 Hong, S.-Y., Noh, Y., and Dudhia, J.: A new vertical diffusion package with explicit treatment of entrainment processes. *Mon.*
78 *Wea. Rev.*, 134, 2318–2341, doi: [10.1175/MWR3199.1](https://doi.org/10.1175/MWR3199.1), 2006.
79
80 [Hu, X., Nielsen-Gammon, J. W., and Zhang, F.: Evaluation of three planetary boundary layer schemes in the WRF model. *J.*](#)
81 [Appl. Meteor. Climatol.](#), 49, 1831–1844.
82
83 Hong, S.-Y.: A new stable boundary-layer mixing scheme and its impact on the simulated East Asian summer monsoon, *Quart.*
84 *J. Roy. Meteor. Soc.*, 136, 1481–1496, 2010.
85
86 Huang, M., and Coauthors: Biogenic isoprene emissions driven by regional weather predictions using different initialization
87 methods: case studies during the SEAC4RS and DISCOVER-AQ airborne campaigns, *Geosci. Model Dev.*, 10, 3085–3104,
88 <https://doi.org/10.5194/gmd-10-3085-2017>, 2017.
89
90 Iacono, M. J., Delamere, J. S., Mlawer, E. J., Shephard, M. W., Clough, S. A., and Collins, W. D.: Radiative forcing by long-
91 lived greenhouse gases: Calculations with the AER radiative transfer models, *J. Geophys. Res.*, 113(D13), doi:
92 [10.1029/2008JD009944](https://doi.org/10.1029/2008JD009944), 2008.
93
94 [Jacob, D. J., and Winner, D. A.: Effect of climate change on air quality, *Atmos. Environ.*, 43, 51–63, 2009.](#)
95
96 [Jin, S., Yang, L., Danielson, P., Homer, C., Fry, J., and Xian, G.: A comprehensive change detection method for updating the](#)
97 [National Land Cover Database to circa 2011. *Rem. Sens. Environ.*, 132, 159–175, 2013.](#)
98
99 Kain, J.S.: The Kain-Fritsch convective parameterization: An update, *J. Appl. Meteorol. Climatol.*, 43(1), 170–181, doi:
00 [10.1175/1520-0450\(2004\)043<0170:TKCPAU>2.0.CO;2](https://doi.org/10.1175/1520-0450(2004)043<0170:TKCPAU>2.0.CO;2), 2004.
01
02 Kumar, S. V., and Coauthors: Land Information System – An Interoperable Framework for High Resolution Land Surface
03 Modeling, *Environmental Modeling & Software*, 21, 1402–1415, doi:10.1016/j.envsoft.2005.07.004, 2006
04
05 Lennartson, G. J., and Schwartz, M. D.: The lake breeze-ground-level ozone connection in eastern Wisconsin: A climatological
06 perspective. *Int. J. Climatol.*, 22, 1347–1364, <https://doi.org/10.1002/joc.802>, 2002
07
08 Lyons, W. A., and Olsson, L. E. 1973: Detailed mesometeorological studies of air pollution dispersion in the Chicago lake
09 breeze. *Mon. Wea. Rev.*, 101, 387–403, [https://doi.org/10.1175/1520-0493\(1973\)101<0387:DMSOAP>2.3.CO;2](https://doi.org/10.1175/1520-0493(1973)101<0387:DMSOAP>2.3.CO;2), 1973
10
11 Mlawer, E. J., Taubman, S. J., Brown, P. D., Iacono, M. J., and Clough, S. A.: Radiative transfer for inhomogeneous
12 atmospheres: Rrtm, a validated correlated-k model for the longwave, *J. Geophys. Res.*, 102(D14), 16663–16682, doi:
13 [10.1029/97JD00237](https://doi.org/10.1029/97JD00237), 1997.
14
15 Morrison, H., Curry, J. A., and Khvorostyanov, V. I.: A new double-moment microphysics parameterization for application
16 in cloud and climate models. Part 1: Description, *J. Atmos. Sci.*, 62, 1665–1677, doi: [10.1175/JAS3446.1](https://doi.org/10.1175/JAS3446.1), 2005.
17

- 18 NCEI: May 2017 national climate report, <https://www.ncei.noaa.gov/access/monitoring/monthly-report/national/201705>,
19 2017, last accessed 09 May 2022.
- 21 Odman, M. T., and Coauthors: Examination of nudging schemes in the simulation of meteorology for use in air quality
22 experiments: Application in the Great Lakes Region, *Journal of Applied Meteorology and Climatology*, 58, 2421-2436, 2019.
- 23
24 Otte, T. L., Nolte, C. G., Otte, M. J., and Bowden, J. H.: Does nudging squelch the extremes in regional climate modeling? *J.*
25 *Clim.*, 25, 7046-7066, doi: [10.1175/JCLI-D-12-00048.1](https://doi.org/10.1175/JCLI-D-12-00048.1), 2012.
- 26
27 Otte, T. L.: The impact of nudging in the meteorological model for retrospective air quality simulations. Part I: evaluation
28 against national observation networks, *J. Appl. Met. Clim.*, 47, 1853-1867, doi: [10.1175/2007JAMC1790.1](https://doi.org/10.1175/2007JAMC1790.1), 2008a.
- 29
30 Otte, T. L.: The impact of nudging in the meteorological model for retrospective air quality simulations. Part II: evaluating
31 collocated meteorological and air quality observations, *J. Appl. Met. Clim.*, 47, 1868-1887, doi: [10.1175/2007JAMC1791.1](https://doi.org/10.1175/2007JAMC1791.1),
32 2008b.
- 33
34 Pierce, R. B., Harkey, M. Lenzen, A., Cronce, L. M., Otkin, J. A., Case, J. L., Henderson, D. S., Adelman, Z., Nergui, T., and
35 Hain, C. R.: High resolution CMAQ simulations of ozone exceedance events during the Lake Michigan Ozone Study.
36 Submitted to *Atmos. Chem. Phys.*, 2023.
- 37
38 Pleim, J. E.: A combined local and nonlocal closure model for the atmospheric boundary layer. Part 1: Model description and
39 testing, *J. Appl. Meteorol. Climatol.*, 46, 1383-1395, doi: [10.1175/JAM2539.1](https://doi.org/10.1175/JAM2539.1), 2007.
- 40
41 Pleim, J. E. and Gilliam, R.: An indirect data assimilation scheme for deep soil temperature in the Pleim-Xiu land surface
42 model. *J. Appl. Meteorol. Climatol.*, 48, 1362-1376, doi: [10.1175/2009JAMC2053.1](https://doi.org/10.1175/2009JAMC2053.1), 2009.
- 43
44 Pleim, J. E., and Xiu, A.: Development of a land surface model. Part II: data assimilation, *J. Appl. Meteorol.*, 42, 1811-1822,
45 [https://doi.org/10.1175/1520-0450\(2003\)042<1811:DOALSM>2.0.CO;2](https://doi.org/10.1175/1520-0450(2003)042<1811:DOALSM>2.0.CO;2), 2003.
- 46
47 [Porter, W. C. and Heald, C. L.: The mechanisms and meteorological drivers of the summertime ozone-temperature
48 relationship, *Atmos. Chem. Phys.*, 19, 13367-13381, <https://doi.org/10.5194/acp-19-13367-2019>, 2019.](https://doi.org/10.5194/acp-19-13367-2019)
- 49
50 Powers, J. G., and Coauthors. The weather research and forecasting model: Overview, system efforts, and future directions.
51 *Bull. Amer. Meteor. Soc.*, 98, 1717-1737, <https://doi.org/10.1175/BAMS-D-15-00308.1>, 2017.
- 52
53 [Pusede, S. E., et al.: On the temperature dependence of organic reactivity, nitrogen oxides, ozone production, and the impact
54 of emission controls in San Joaquin Valley, California, *Atmos. Chem. Phys.*, 14, 3373-3395, 2014.](https://doi.org/10.5194/acp-14-3373-2014)
- 55
56 Ragland, K. and Samson, P.: Ozone and visibility reduction in the Midwest: evidence for large-scale transport. *J. Applied
57 Meteorology*, 16, 1101-1106, 1977.
- 58
59 Santanello, J. A., and Coauthors: Land-atmosphere interactions the LoCo perspective, *Bull. Am. Meteorol. Soc.*, 99, 1253-
60 1272. <https://doi.org/10.1175/BAMS-D-17-0001.1>, 2018.
- 61
62 Santanello Jr., J. A., Lawston, P., Kumar, S., and Dennis, E.: Understanding the impacts of soil moisture initial conditions on
63 NWP in the context of land-atmosphere coupling, *J. Hydrometeorol.*, 20, 793-819. <https://doi.org/10.1175/JHM-D-18-0186.1>,
64 2019.
- 65
66 Schwab, D. J., Leshkevich, G. A., and Muhr, G. C.: Satellite measurements of surface water temperature in the Great Lakes:
67 Great Lakes Coast Watch, *Journal of Great Lakes Research*, 18, 247-258, 1992.
- 68

69 Schwingshackl, C., Hirschi, M., Seneviratne, S.I.: Quantifying spatiotemporal variations of soil moisture control on surface
70 energy balance and near-surface air temperature, *J. Climate*, 30, 7105–7124. <https://doi.org/10.1175/JCLI-D-16-0727.1>, 2017.

71
72 Stanier, C. O., and Coauthors: Overview of the Lake Michigan Ozone Study, *Bull. Am. Meteor. Soc.*, 102, E2208-E2225.

73
74 Sutton, C., Hamill T. M., and Warner T. T.: Will perturbing soil moisture improve warm-season ensemble forecasts? A proof
75 of concept, *Mon. Wea. Rev.*, 134, 3174–3189, 2006.

76
77 Thompson, G., Field, P. R., Rasmussen, R. M., and Hall, W. D.: Explicit forecasts of winter precipitation using an improved
bulk microphysics scheme. Part II: Implementation of a new snow parameterization, *Mon. Wea. Rev.*, 136, 5095–5115, 2008.

78
79 Thompson, G., Tewari, M., Ikeda, K., Tessorof, S., Weeks, C., Otkin, J., Kong, F.: Explicitly-coupled cloud physics and
radiation parameterizations and subsequent evaluation in WRF high-resolution convective forecasts. *Atmos. Res.*, 168, 92-
80 104, doi:[10.1016/j.atmosres.2015.09.005](https://doi.org/10.1016/j.atmosres.2015.09.005), 2016.

81
82 [Torres-Vazquez, A., Pleim, J., Gilliam, R., Pouliot, G.: Performance evaluation of the meteorology and air quality conditions](https://doi.org/10.1029/2021JD035890)
83 [from multiscale WRF-CMAQ simulations for the Long Island Sound Tropospheric Ozone Study \(LISTOS\). *J. Geophys. Res.*](https://doi.org/10.1029/2021JD035890)
84 [Atmos., 127, e2021JD035890. <https://doi.org/10.1029/2021JD035890>, 2022.](https://doi.org/10.1029/2021JD035890)

85
86 Welty, J., and Zeng, X.: Does soil moisture affect warm season precipitation over the Southern Great Plains?, *Geophys. Res.*
87 *Let.*, 45, 7866–7873. <https://doi.org/10.1029/2018GL078598>, 2018

88
89 Vargas, M., Jiang, Z., Ju, J., and Csizsar, I. A.: Real-time daily rolling weekly Green Vegetation Fraction (GVF) derived from
the Visible Imaging Radiometer Suite (VIIRS) sensor onboard the SNPP satellite. Preprints, 20th Conf. Satellite Meteorology
90 and Oceanography, Phoenix, AZ, Amer. Meteor. Soc., P210. [Available online at
91 ams.confex.com/ams/95Annual/webprogram/Paper259494.html], 2015, last accessed 09 May 2022.

92
93
94 Wang, X., Parrish, D., Kleist, D., and Whitaker, J.: GSI 3DVar-based Ensemble-variational hybrid data assimilation for NCEP
95 Global Forecast System: Single-resolution experiments, *Mon. Wea. Rev.*, 141, 4098-4117, doi:10.1175/MWR-D-12-00141.1,
96 2013.

97
98 [Wang, Y., Lin, N., Li, W., Guenther, A., Lam, J. C. Y., Tai, A. P. K., Potosnak, M. J., and Seco, R.: Satellite-derived constraints](https://doi.org/10.5194/acp-22-14189-2022)
99 [on the effect of drought stress on biogenic isoprene emissions in the southeastern US. *Atmos. Chem. Phys.*, 22, 14189–14208,](https://doi.org/10.5194/acp-22-14189-2022)
100 <https://doi.org/10.5194/acp-22-14189-2022>, 2022.

101
102 [Wiedinmyer, C., Tie, X., Guenther, A., Neilson, R., and Granier, C.: Future Changes in Biogenic Isoprene Emissions: How](https://doi.org/10.1029/2006GL022801)
103 [Might They Affect Regional and Global Atmospheric Chemistry?. *Earth Interact.*, 10, 1–19, 2006.](https://doi.org/10.1029/2006GL022801)

104
105 Xia, Y., and Coauthors: Continental-scale water and energy flux analysis and validation for the North-American Land Data
106 Assimilation System Project Phase 2 (NLDAS-2), Part 1: Intercomparison and application of model products, *J. Geophys.*
107 *Res. Atmos.*, 117(D03109), doi:10.1029/2011JD016048, 2012.

108
109 Xiu, A., and Pleim, J. E.: Development of a land surface model. Part 1: Application in a mesoscale meteorological model, *J.*
110 *Appl. Meteor.*, 40, 192-209, doi: [10.1175/1520-0450\(2001\)040<0192:DOALSM>2.0.CO;2](https://doi.org/10.1175/1520-0450(2001)040<0192:DOALSM>2.0.CO;2), 2001.

11
12 Yin, J., Zhan, X., Zheng, Y., Hain, C. R., Ek, M., Wen, J., Fang, L., and Liu, J.: Improving Noah land surface model
13 performance using near real time surface albedo and green vegetation fraction. *Agric. For. Meteorol.*, 218-219, 171–183,
14 <https://doi.org/10.1016/j.agrformet.2015.12.001>, 2016.

15
16 Zhang, J., and Coauthors: Multi-Radar Multi-Sensor (MRMS) Quantitative Precipitation Estimation: Initial operating
17 capabilities, *Bull. Amer. Meteor. Soc.*, 97, 621-637, doi:10.1175/BAMS-D-14-00174.1, 2016.

18